JCI The Journal of Clinical Investigation

A20 regulates lymphocyte adhesion in murine neuroinflammation by restricting endothelial ICOSL expression in the CNS

Lisa Johann, … , Markus Schwaninger, Ari Waisman

J Clin Invest. 2023. https://doi.org/10.1172/JCI168314.

Research In-Press Preview Autoimmunity Neuroscience

Graphical abstract

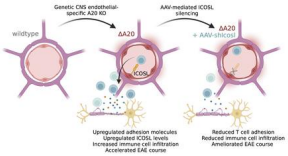

A20 regulates lymphocyte adhesion in murine neuroinflammation by restricting endothelial ICOSL expression in the CNS

Lisa Johann[1], Sasha Soldati[2], Kristin Müller[3], Josephine Lampe[3,4], Federico Marini[5,6], Matthias Klein[7], Eva Schramm[1], Nathalie Ries[1], Carsten Schelmbauer[1], Ilaria Palagi[1], Khalad Karram[1], Julian C. Assmann[3], Mahtab A. Khan[3], Jan Wenzel[3,4], Mirko H. H. Schmidt[8], Jakob Körbelin[9], Dirk Schlüter[10], Geert van Loo[11,12], Tobias Bopp[6,7], Britta Engelhardt[2], Markus Schwaninger[3,4] and Ari Waisman[1,6]

[1] Institute for Molecular Medicine, University Medical Center of the Johannes Gutenberg University Mainz, Mainz, Germany

[2] Theodor Kocher Institute, University of Bern, Bern, Switzerland

[3] Institute for Experimental and Clinical Pharmacology and Toxicology, Center of Brain, Behavior and Metabolism (CBBM), University of Lübeck, Lübeck, Germany

[4] DZHK (German Research Centre for Cardiovascular Research), Hamburg-Lübeck-Kiel, Germany

[5] Institute of Medical Biostatistics, Epidemiology and Informatics (IMBEI), University Medical Center of the Johannes Gutenberg University Mainz, Mainz, Germany

[6] Research Center for Immunotherapy (FZI), University Medical Center of the Johannes Gutenberg University Mainz, Mainz, Germany

[7] Institute for Immunology, University Medical Center of the Johannes Gutenberg University Mainz, Mainz, Germany

[8] Institute of Anatomy, Medical Faculty Carl Gustav Carus, Technische Universität Dresden School of Medicine, Dresden, Germany

[9] University Medical Center Hamburg-Eppendorf, Department of Oncology, Hematology and Bone Marrow Transplantation, Hamburg, Germany

[10] Hannover Medical School, Institute of Medical Microbiology and Hospital Epidemiology, Hannover, Germany

[11] Department of Biomedical Molecular Biology, Ghent University, Ghent, Belgium

[12] VIB-UGent Center for Inflammation Research, Ghent, Belgium

Corresponding author:

Ari Waisman

Institute for Molecular Medicine, University Medical Center of the Johannes Gutenberg University Mainz, Langenbeckstraße 1, 55131 Mainz, Germany

(+49) 6131-17-9129

waisman@uni-mainz.de

Conflict of interest:

JK is listed as inventor of a patent on AAV-BR1, held by Boehringer Ingelheim International GmbH (patent no. US10696717B2). There are no other conflicts of interest to declare.

ABSTRACT

A20 is a ubiquitin-modifying protein that negatively regulates NF-κB signaling. Mutations in A20/*TNFAIP3* are associated with a variety of autoimmune diseases, including multiple sclerosis (MS). We found that deletion of A20 in central nervous system (CNS) endothelial cells (ECs) enhances experimental autoimmune encephalomyelitis (EAE), a mouse model of MS. $A20^{\Delta CNS\text{-}EC}$ mice showed increased numbers of CNS-infiltrating immune cells during neuroinflammation and in the steady state. While the integrity of the blood-brain barrier (BBB) was not impaired, we observed a strong activation of CNS-ECs in these mice, with dramatically increased levels of the adhesion molecules ICAM-1 and VCAM-1. We discovered ICOSL as adhesion molecule expressed by A20-deficient CNS-ECs. Silencing of ICOSL in CNS microvascular ECs partly reversed the phenotype of $A20^{\Delta CNS\text{-}EC}$ mice without reaching statistical significance and delayed the onset of EAE symptoms in wildtype mice. In addition, blocking of ICOSL on primary mouse brain microvascular endothelial cells (pMBMECs) impaired the adhesion of T cells in vitro. Taken together, we here propose that CNS EC-ICOSL contributes to the firm adhesion of T cells to the BBB, promoting their entry into the CNS and eventually driving neuroinflammation.

INTRODUCTION

Multiple sclerosis (MS) is the most prevalent chronic inflammatory disease of the central nervous system (CNS) in young adults (1). To date, the causes of MS are not fully understood, yet it is presumed to be an autoimmune disease driven by autoreactive T cells targeting CNS antigens (2). Upon reactivation at the CNS borders, autoreactive immune cells infiltrate the CNS parenchyma and attack the myelin sheaths that surround neurons, eventually leading to axonal loss and causing neuroinflammation (3,4).

Transmigration of T cells across the blood-brain barrier (BBB) represents a key step in the pathology of MS and its animal model experimental autoimmune encephalomyelitis (EAE) (5), which follows a multistep process involving interaction of different adhesion molecules with integrins (6,7). While expression of these molecules on the BBB is usually low, pro-inflammatory cytokine signaling during neuroinflammation induces dramatic brain microvascular endothelial cell (BMEC) activation (8-12). IL-1 signaling is an essential pathway driving the expression of adhesion molecules like intercellular adhesion molecule 1 (ICAM-1) and vascular cell adhesion molecule 1 (VCAM-1) on BMECs through nuclear translocation of nuclear factor ‘kappa-light-chain-enhancer’ of activated B cells (NF-κB), thus promoting the firm adhesion of leukocytes to the BBB (13-18).

A20 is an integral molecule for the negative regulation of the NF-κB signaling pathway. The transcription factor NF-κB is active in BMECs in a variety of conditions associated with vascular dysfunction and BBB impairment (19-21). Moreover, a protective role was ascribed to the NF-κB essential modulator (NEMO) and the upstream kinase TAK1 in BMECs, as their deletion causes BBB disruption and BMEC cell death partly mediated by TNF signaling (22). Importantly, A20 is well-known to counteract the cytotoxic effects of TNF (23-25).

Genetic variations in the *TNFAIP3* gene, encoding for A20, have been linked to the susceptibility to MS (26). Interestingly, mice deficient for A20 develop a spontaneous neuroinflammation with remarkable micro- and astrogliosis as well as BMEC activation (27). Deletion of A20 specifically in astrocytes or microglia further proved the protective function of A20 in the establishment of active EAE and spontaneous neuroinflammation (28-30). Besides glial cells, also ECs express high levels of A20 in the steady state condition (31), yet studies regarding the role of A20 in CNS-ECs are so far lacking.

We found that mice lacking A20 in CNS-ECs develop an exacerbated EAE disease upon adoptive transfer (AT) of encephalitogenic T cells. While we did not observe pronounced alterations in the structure of the microvasculature or BBB integrity, we found that loss of A20 in CNS-ECs dramatically upregulates ICAM-1, VCAM-1 and the Inducible T cell co-stimulator ligand (ICOSL). Using a CNS-microvasculature endothelial cell-specific viral vector to silence ICOSL, we could partly rescue the more severe AT-EAE course in $A20^{\Delta CNS\text{-}EC}$ mice and delay the onset of an active EAE disease in wildtype mice. Mechanistically, we demonstrate that ICOSL drives the adhesion of Th1 and Th17 cells to an in vitro BBB model. Taken together, our work reveals A20-regulated ICOSL as an adhesion molecule involved in the multi-step transmigration process of T cells across the BBB under inflammatory conditions.

RESULTS

Mice with A20-deficient CNS-ECs are hypersensitive to adoptive transfer experimental autoimmune encephalomyelitis

To investigate the involvement of CNS-endothelial A20 in autoimmune neuroinflammation we generated $A20^{\Delta CNS\text{-}EC}$ mice which lack A20 in CNS-ECs upon tamoxifen (TAM)-inducible Cre

recombination (Figure 1A). RT-PCR and Western blot analyses of primary mouse brain microvascular endothelial cells (pMBMECs) confirmed the deletion of *Tnfaip3*/A20 (Figure 1B, C). To our surprise, we did not observe a difference in disease severity between $A20^{\Delta CNS\text{-}EC}$ mice and littermate controls in three different active EAE models where mice were immunized with $MOG_{35\text{-}55}$ in complete Freund's adjuvant (CFA) (Supplemental Figure 1A-L). As CFA is known to activate CNS-ECs (13), we next studied the phenotype of $A20^{\Delta CNS\text{-}EC}$ mice in an adoptive transfer (AT)-EAE model which circumvents CFA-driven effects.

Interestingly, we found that compared to littermate controls, the majority of $A20^{\Delta CNS\text{-}EC}$ mice developed EAE symptoms (Figure 1D). This resulted in an increased average disease severity, with increased area under the curve (AUC) values and maximum scores (Figure 1E-G). $A20^{\Delta CNS\text{-}EC}$ mice furthermore showed a tendency towards earlier disease onset (Figure 1H). To exclude astrocytic contamination as previously reported for the Slco1c1-$CreER^{T2}$ mouse line (32) we generated mice lacking A20 in all endothelial cells ($A20^{\Delta EC}$) by crossing $A20^{fl/fl}$ mice to Cdh5(PAC)-$CreER^{T2}$ mice (33) to validate our data. Indeed, we observed a very similar phenotype with an overall increased disease severity (Figure 1I-K). $A20^{\Delta EC}$ mice furthermore showed a significantly accelerated disease onset, with mice developing symptoms in average two days earlier than controls (Figure 1L).

We next focused on a different model involving CNS inflammation and used an MCAO model to induce stroke in $A20^{\Delta CNS\text{-}EC}$ mice. We observed significantly increased infarct and edema volumes, overall leading to a mildly increased edema-corrected infarct volume in $A20^{\Delta CNS\text{-}EC}$ mice (Supplemental Figure 2). Together, this data strongly suggests a protective role for CNS EC-A20 in CNS autoimmunity and sterile inflammation.

Loss of A20 in CNS-ECs drives immune cell infiltration into the CNS

To investigate the extent of leukocyte infiltration, we isolated immune cells from the SC at the peak of AT-EAE disease and analyzed cell subsets and cytokine production by flow cytometry after antigen recall (Figure 2A). We found dramatically increased numbers of $CD45.1^+$ transferred and amongst them $CD40L^+$ MOG_{35-55} -specific T cells in $A20^{\Delta CNS\text{-}EC}$ mice (Figure 2B, C). Also, the number of cytokine-producing cells was significantly increased (Figure 2D-F). Furthermore, absolute cell counts of dendritic cells, neutrophils and monocytes were elevated in $A20^{\Delta CNS\text{-}EC}$ mice (Supplemental Figure 3A-E). We next analyzed the location of $CD3^+$ T cells in the SC by immunostaining. Compared to controls, we found high numbers of T cells in the SC of $A20^{\Delta CNS\text{-}EC}$ mice, with cells forming perivascular cuffs but also penetrating deep into the parenchyma (Figure 2G). As EAE disease severity is strongly dependent on the ratio of effector to regulatory T cells (Treg cells) (34), we next assessed if loss of A20 in CNS-ECs influences Treg cell frequencies. We did not observe changes in Treg cell frequencies or effector T cell to Treg cell ratio at day post transfer (DPT) 18 (Supplemental Figure 4A-D). Based on these observations, we conclude that the loss of A20 in CNS-ECs promotes immune cell infiltration across the BBB under inflammatory conditions without affecting the proportion of effector T cells to Treg cells.

We next addressed the question whether loss of A20 in CNS-ECs causes infiltration of immune cells even in the absence of exogenously induced inflammation. We assessed the numbers of $CD45^+$ total infiltrates, $TCR\beta^+$ T cells and $CD11b^+$ myeloid cells in the steady state CNS one week after TAM injection. Indeed, we found increased numbers of immune cells infiltrating the CNS in $A20^{\Delta CNS\text{-}EC}$ mice in the steady state compared to littermate controls (Figure 2H-J, Supplemental Figure 3F, G). Interestingly, the frequencies of $TCR\beta^+$ T cells and $CD11b^+$ myeloid cells amongst all infiltrating cells were not altered (Supplemental Figure 3H). Taken together,

this data suggests that the loss of A20 in CNS-ECs provokes the infiltration of immune cells across the BBB even in the absence of an inflammatory stimulus.

A20 protects from excessive adhesion molecule expression in steady state CNS-ECs

To test whether deficiency for A20 in BMECs results in CNS blood vessel abnormalities, we performed immunostainings of the endothelial cell marker CD31 and of collagen IV as an integral basement membrane component. We neither observed alterations in vessel length nor increased numbers of empty basement membrane strands, also known as string vessels (35), in the brains of $A20^{\Delta CNS\text{-}EC}$ mice (Figure 3A, B). We next focused on BBB integrity in $A20^{\Delta CNS\text{-}EC}$ mice. By performing immunostaining for the tight junction molecule occludin, we observed reduced fluorescence intensity in BMECs of $A20^{\Delta CNS\text{-}EC}$ mice (Figure 3E, F). However, brain weight, as an indicator of brain edema, was not increased compared to controls (Figure 3D). To exclude a disruption of the BBB and the blood-spinal cord barrier (BSCB), we assessed the integrity by injecting a small 3-5 kDa dextran tracer and measuring fluorescence in brain or SC. Compared to mice at the peak of an active EAE disease, in which BBB and BSCB integrity are compromised, $A20^{\Delta CNS\text{-}EC}$ mice did not show an increased permeability for FITC-dextran, confirming normal BBB and BSCB integrities (Figure 3G, H).

As T cell transmigration across the BBB is mainly dependent on the surface expression levels of adhesion molecules (36), we next investigated if the increased numbers of immune cells infiltrating the CNS in $A20^{\Delta CNS\text{-}EC}$ mice were due to alterations in adhesion molecule expression. By performing immunostaining of VCAM-1 together with collagen IV, we detected dramatically increased numbers of $VCAM\text{-}1^{+}$ microvessels in the brain cortex of $A20^{\Delta CNS\text{-}EC}$ mice (Figure 4A, B). Also, ICAM-1 levels were dramatically increased on CNS microvessels in $A20^{\Delta CNS\text{-}EC}$ mice, with almost 100% of CNS-ECs expressing ICAM-1 (Figure 4C-F). Both molecules are

well-known to mediate the multistep process of immune cell transmigration across the BBB (6). Our data suggests that loss of A20 in CNS-ECs does not influence BBB integrity but causes a dramatic upregulation of cell adhesion molecules, which at least partially drives leukocyte infiltration and AT-EAE severity.

RNA-seq reveals strong activation of CNS-ECs in A20$^{\Delta CNS\text{-}EC}$ mice

Blocking immune cell infiltration by targeting α4-integrin, a binding partner of VCAM-1, with natalizumab is an effective treatment option for MS patients presenting with a relapsing-remitting disease course (37-39). Yet, this therapeutic strategy comes with a risk to develop severe CNS infections (40). Identification of novel adhesion molecules facilitating the extravasation of specific cell subsets is thus essential. We therefore made use of the A20$^{\Delta CNS\text{-}EC}$ mice to characterize their CNS-EC adhesion molecule profile in-depth by RNA sequencing. Crossing these mice to R26R-EYFP reporter mice allowed us to sort for CNS-ECs from the SC with Cre-mediated recombination, which could be observed in approximately 90% of all ECs (Supplemental Figure 5A, B). To focus on molecules involved in immune cell transmigration, we included a control group of wildtype-like A20$^{fl/fl}$ mice at day post immunization (DPI) 10 of an active EAE disease, a timepoint where immune cell extravasation across the BBB is known to happen (41). We first confirmed the purity of the sorted SC-ECs by plotting endothelial marker genes as well as genes specific for other CNS-resident cells (Figure 5A). We next focused on genes that were differentially expressed (DE) in either the A20$^{\Delta CNS\text{-}EC}$-eYFP or the EAE group compared to the control condition, respectively. While most of the DE genes were found in the EAE situation, a substantial amount of DE genes could also be identified in A20$^{\Delta CNS\text{-}EC}$-eYFP mice (Figure 5B). The overlap of DE genes in the A20$^{\Delta CNS\text{-}EC}$-eYFP and the EAE condition resulted in 26 genes that were commonly upregulated and 4 genes that were

commonly downregulated (Figure 5C, D). Amongst these genes, *Icam1* and *Vcam1* represented the top upregulated genes, confirming our previous findings. Also, *Tnfaip3* itself was among the upregulated genes, yet mapping the reads of *Tnfaip3* to the genetic locus confirmed the excision of exon 3 in $A20^{\Delta CNS\text{-}EC}$ mice, rendering the transcript non-translatable (Supplemental Figure 5C) (42). To investigate if other genes related to immune cell transmigration across the BBB were amongst the commonly DE genes, we performed a KEGG pathway analysis. The most prominent pathways were the inflammatory *NF-κB* and *TNF signaling pathways*, pointing out the essential function of A20 as negative regulator of these signaling cascades. Interestingly, and as hypothesized, also the *Cell adhesion molecules* pathway was amongst the top KEGG terms (Figure 5E). This was further underscored by a Gene Ontology (GO) term analysis, in which *Leukocyte cell-cell adhesion*, *Membrane to membrane docking* and *Cell adhesion* represented the top affected Biological Processes (Suppl. Figure 5D).

ICOSL is upregulated on CNS-ECs under inflammatory conditions

Interestingly, besides *Icam1* and *Vcam1* also *Icosl* was identified as cell adhesion molecule in the KEGG pathway analysis and moreover, *Icosl* expression levels in $A20^{\Delta CNS\text{-}ECs}$ and DPI10 ECs were very similar to those of *Icam1* and *Vcam1* (Supplemental Figure 5E). RT-PCR validation of *Icosl* expression indeed confirmed its upregulation in sorted CNS-ECs from naïve $A20^{\Delta CNS\text{-}EC}$ mice compared to littermate controls (Supplemental Figure 5F). In addition, we could validate the upregulation of ICOSL protein on CNS-ECs in vivo during EAE (Figure 5F, G).

Expression of ICOSL on peripheral ECs as well as on the human BMEC-derived cell line hCMEC/D3 is strongly upregulated by various inflammatory stimuli in vitro (43,44). We thus

investigated *Icosl* mRNA levels in pMBMECs isolated from $A20^{\Delta CNS\text{-}EC}$ mice and found increased levels in response to TNF stimulation compared to unstimulated or TNF-stimulated $A20^{fl/fl}$ control pMBMECs (Supplemental Figure 5G). Furthermore, while TNF stimulation of wildtype pMBMECs significantly increases *Icosl* expression, IL-1β stimulation led to an even higher upregulation of *Icosl* mRNA levels (Supplemental Figure 5H). Moreover, ICOSL upregulation in response to IL-1β stimulation followed a very similar pattern like ICAM-1 and VCAM-1 (Supplemental Figure 5I). These data indicate that in addition to ICAM-1 and VCAM-1, also ICOSL is upregulated on CNS-ECs under inflammatory conditions and may therefore contribute to the onset of neuroinflammation.

Silencing of CNS microvascular EC-ICOSL ameliorates AT-EAE in $A20^{\Delta CNS\text{-}EC}$ mice

To evaluate the function of CNS EC-ICOSL in autoimmune neuroinflammation, we knocked down ICOSL by delivering shRNA to CNS microvascular ECs using the AAV-BR1. As not 100% of CNS microvascular ECs are transduced upon AAV-BR1 application (45), we first confirmed that the location of the transduced ECs was in close proximity to the infiltrating immune cells during EAE. Indeed, we found multiple GFP^+ vessels in close proximity to $CD3^+$ T cells in the perivascular space, but also in close proximity to T cells infiltrating into the SC parenchyma in EAE mice treated with AAV-BR1-eGFP (Figure 6A, B). Immunofluorescence furthermore proved specificity of the AAV-BR1-eGFP in targeting vessels, as eGFP only co-localized with laminin but not cortical neuronal NeuN (Supplemental Figure 6A). Next, we designed a CNS microvascular EC-specific AAV carrying either an shRNA against *Icosl* (AAV-BR1-shIcosl) or a scrambled shRNA (AAV-BR1-con) (Figure 6C). Both constructs express a GFP reporter under the relatively weak RSV promoter, which was chosen to exclude potential GFP-induced cytotoxicity (46). Yet, GFP intensity was still strong enough to validate the target specificity.

Upon injection of the AAV-BR1-shIcosl construct, GFP^+ cells could only be found among the $CD31^+$ $Ly6C^+$ EC population, but not in other CNS-resident cells (Supplemental Figure 6B-F). Transduction of pMBMECs with AAV-BR1-shIcosl furthermore proved the efficiency of this virus to knockdown *Icosl* as expression levels were reduced by approximately 70% in IL-1β stimulated pMBMECs (Supplemental Fig 6G). Flow cytometry of CNS-ECs upon in vivo administration of AAV-BR1-shIcosl furthermore demonstrated a significant reduction in the mean fluorescence intensity of ICOSL as well as in the percentage of $ICOSL^+$ ECs in mice after immunization with MOG_{35-55}/CFA (Figure 6D, E). Of note, treatment with AAV-BR1-shIcosl did not influence protein levels of ICAM-1 or VCAM-1 in CNS-ECs (Supplemental Figure 6H, I).

We next used this system to knockdown ICOSL in CNS microvascular ECs in $A20^{\Delta CNS\text{-}EC}$ mice to evaluate the contribution of ICOSL to their increased EAE phenotype. Administration of AAV-BR1-shIcosl, but not AAV-BR1-con, mildly ameliorated the AT-EAE disease course including the area under the curve, the day of onset and the score at DPT7, a timepoint shortly after disease onset (Figure 6F-I). Furthermore, AAV-BR1-shIcosl administration significantly reduced the number of transferred $CD45.1^+$ T cells infiltrating into the SC (Figure 6J). Thus, ICOSL participates in driving autoimmune neuroinflammation in $A20^{\Delta CNS\text{-}EC}$ mice and its knockdown reduces the infiltration of encephalitogenic cells into the CNS.

Endothelial ICOSL influences day of active EAE onset in wildtype mice

Next, we wanted to recapitulate our findings in wildtype mice in an active EAE model. For this, AAV-BR1-shIcosl was injected i.v. and two weeks later mice were immunized with MOG_{35-55} in CFA. Confirming our previous findings, we also detected a mildly ameliorated disease and a tendency towards reduced numbers of infiltrating immune cells in mice treated with AAV-

BR1-shIcosl (Figure 6K-O). More importantly, disease onset could be delayed by an average of two days in the AAV-BR1-shIcosl treated group (Figure 6M). These findings confirm a functional role for CNS microvascular EC-ICOSL in driving autoimmune neuroinflammation, possibly by promoting the infiltration of pathogenic T cells.

ICOSL promotes T-cell adhesion to the BBB in vitro

ICOSL is an immunoglobulin superfamily member, expressing immunoglobulin-like domains that are known to mediate cell-cell adhesion through binding in a homophilic or heterophilic manner (47). ICOSL thus shares structural similarities with the known adhesion molecules ICAM-1, VCAM-1 and the more recently characterized molecules activated leukocyte adhesion molecule (ALCAM-1), melanoma cell adhesion molecule (MCAM-1) and dual immunoglobulin-domain containing cell adhesion molecule (DICAM-1) (48-52). Recently, it was shown that ICOSL can bind to $\alpha_V\beta_3$, an integrin known to be important for EAE development by mediating the recruitment of encephalitogenic T cells to the CNS (53,54). This body of evidence led us to hypothesize that CNS EC-ICOSL could be involved in mediating immune cell adhesion to the BBB. To prove this, we performed T cell migration assays as well as static T cell adhesion assays on anti-ICOSL-treated pMBMECs. We found significantly reduced numbers of adhering MOG_{35-55}-specific Th1 and Th17 cells under static conditions when ICOSL was blocked on IL-1β-stimulated pMBMECs (Figure 7A-C). We next assessed the post-arrest behavior of Th1 cells under physiological flow conditions. The numbers of arrested T cells showed a trend towards lower numbers of cells arresting when ICOSL was blocked, however, due to the variance across the individual experiments not reaching statistical significance (Figure 7D). The post-arrest behavior, which we categorized into fractions of T cells that were detaching, probing, probing followed by diapedesis, crawling and crawling followed by diapedesis, was unaltered when

ICOSL was blocked (Figure 7E). Also, the crawling distance and crawling speed of the T cells that successfully performed diapedesis following crawling on the pMBMECs was not changed (Figure 7F, G). Taken together, ICOSL promotes the arrest of Th1 and Th17 cells to the monolayer without influencing the post-arrest behavior of T cells on pMBMECs under physiological flow.

DISCUSSION

In this study, we identified a previously unknown role of CNS-EC A20 in neuroinflammation. Our results show that the loss of A20 in CNS-ECs strongly increased the risk to develop EAE upon transfer of encephalitogenic T cells into naïve recipients and accelerates disease onset. ECs lacking A20 were dramatically activated which resulted in the upregulation of cell adhesion molecules like ICAM-1 and VCAM-1 but also ICOSL. We propose here that A20 serves as a gatekeeper for the activation of ECs, and its absence drives transmigration of encephalitogenic T cells across the BBB and by this, at least partially, contributes to the increased disease susceptibility.

Supporting evidence for this hypothesis comes from the observation that innate immune activation, for example mediated by CFA used in the active EAE induction protocol, drives endothelial activation and promotes upregulation of adhesion molecules already before onset of disease, suggesting a causal role for endothelial activation in disease initiation (13,55,56). Interestingly, and in contrast to A20-deficiency in microglia and astrocytes (28,29), we did not observe alterations in an actively induced EAE disease in mice with A20-deficient ECs. It seems likely that the endothelial activation in response to CFA in the active EAE model masks the effects driven by A20 deletion in CNS-ECs and could thus explain the difference seen in AT-EAE but not active EAE outcomes.

We observed an increased infiltration of immune cells into the CNS of $A20^{\Delta CNS\text{-}EC}$ mice in steady state and after AT-EAE. To enter the CNS, immune cells need to cross the BBB, which represents a key step in the pathology of CNS autoimmune diseases such as MS. Both immune cells and BMECs require a certain state of activation to allow immune cells to cross the BBB. The influence of cytokines and other inflammatory mediators secreted by activated T cells but also innate immune cells on the endothelium has been extensively described (57-59). In particular, pro-inflammatory cytokines like TNF or IL-1β that activate the NF-κB pathway are essential in mediating the upregulation of cell adhesion molecules on BMECs which promote the infiltration of pathogenic T cells and the development of CNS autoimmunity (13,60,61). Upregulation of ICAM-1 and VCAM-1 in CNS-ECs has been described in $A20^{-/-}$ mice in the steady-state, however, it was suggested that this upregulation of adhesion molecules was due to the overall heightened cerebral inflammation present in $A20^{-/-}$ mice (27). Opposingly, we show here that ICAM-1 and VCAM-1 upregulation in steady-state CNS-ECs was driven by an endothelial-intrinsic response to A20-deficiency, as $A20^{\Delta CNS\text{-}EC}$ mice manifested a strong expression of both molecules without external inflammatory stimulation.

Our results furthermore indicate that rather excessive adhesion molecule expression and not BBB breakdown are responsible for the pronounced CNS immune cell infiltration in $A20^{\Delta CNS\text{-}EC}$ mice. It was earlier proposed that NF-κB signaling in BMECs is essential for maintaining barrier integrity (22). Disruption of NF-κB signaling through CNS EC-specific deletion of NEMO or TAK1 resulted in an increased BBB permeability which was suggested to result from impaired A20-mediated occludin stabilization (22). Although we could confirm that A20-deficiency in CNS-ECs leads to decreased occludin levels, this reduction did not cause BBB or BSCB breakdown in our study, underscoring the debate about the necessity of occludin for barrier integrity (62-

65). Our data furthermore corroborates earlier reports of $A20^{-/-}$ and $A20^{+/-}$ mice, which also did not manifest any signs of BBB disruption (27,66). We can thus conclude that activation of BMECs through loss of A20 provokes expression of cell adhesion molecules which promotes the firm adhesion of immune cells to the BBB and facilitates their entry into the CNS.

Supporting our findings, we furthermore found a more severe disease pathology in the MCAO model, a model involving sterile CNS inflammation, in $A20^{\Delta CNS\text{-}EC}$ mice. Interestingly, T cells infiltrate into the injured areas as early as 24h post MCAO induction (67) and blocking of the α4-integrin unit of VLA-4, the binding partner of VCAM-1, reduces the infarct volumes by restricting CNS T cell infiltration (68,69). It is thus possible, that the increased infarct areas in $A20^{\Delta CNS\text{-}EC}$ arise from a more pronounced T cell infiltration due to the massive EC activation.

The success of targeting the VLA-4 subunit α4-integrin with natalizumab in MS therapy points out the attractiveness of interfering with transmigration of immune cells across the BBB in diseases involving CNS inflammation. Yet, due to the potential side effects of this treatment strategy it is necessary to identify alternative targets for therapeutic intervention. In recent years, alternative cell adhesion molecules involved in immune cell transmigration across the BBB have been identified. ALCAM was found to be an important adhesion molecule guiding B cell and monocyte trafficking across the BBB, yet deletion of this molecule dramatically influences the barrier integrity and causes more severe EAE disease (48,49,70). Also, MCAM was implicated in several studies to be essential for $CD8^+$ as well as Th17 cell migration across the BBB (50,51,71). More recently, also DICAM was found to be involved in Th17 cell migration across the BBB and was suggested as a potential target in progressive MS forms (52). While progress has been made in recent years, the spectrum of molecular interactions occurring at the CNS-peripheral interface is certainly not yet disentangled in its entirety. We here identified

A20-regulated ICOSL as adhesion molecule contributing to the firm adhesion of MOG_{35-55} specific pro-inflammatory Th1 and Th17 cells to the BBB. Although the reduction in T cell adhesion when ICOSL was blocked appears rather mild, the effect is in line with studies investigating T cell adhesion to other adhesion molecules (52,72). ICOSL was only recently reported to mediate adhesion of podocytes by binding to the $\alpha_V\beta_3$ integrin through its RGD motif (54). Interestingly, Roussel *et al.* earlier introduced a human mutation in ICOSL, which was found in one patient with a combined immunodeficiency syndrome (73). The authors identified an involvement of endothelial ICOSL in mediating the transmigration of T cells and neutrophils across an in vitro endothelial barrier (73). We here corroborate these findings and extent the involvement of endothelial ICOSL in immune cell adhesion from the periphery to brain-derived pMBMECs. Future studies are, however, necessary to determine the exact binding partner of ICOSL that mediates this adhesion and to further characterize the spectrum of immune cells having the capacity to bind to ICOSL.

We could furthermore underscore the functional role of CNS EC-ICOSL in the development of autoimmune neuroinflammation by in vivo silencing of ICOSL with a CNS-microvascular endothelial specific AAV. Although the GFP signal from our AAV-BR1-shIcosl likely underrepresents the percentage of transduced cells due to the comparably weak RSV promoter driving GFP expression, we could confirm the efficiency of our construct to knock down ICOSL specifically in CNS-ECs both in vitro and in vivo. More importantly, we were able to partly rescue the accelerated disease outcome in $A20^{\Delta CNS\text{-}EC}$ mice by treating them with AAV-BR1-shIcosl, although not reaching statistical significance. Notably, and opposed to observations from Roussel *et al.*, protein levels of ICAM-1 and VCAM-1 molecules were not affected by silencing of ICOSL (73). The high levels of these molecules remaining in $A20^{\Delta CNS\text{-}EC}$

399 mice might explain the rather mild amelioration in the day of disease onset and the overall
400 disease severity upon treatment with AAV-BR1-shIcosl. Nevertheless, silencing of ICOSL on
401 CNS-ECs restricted the infiltration of transferred encephalitogenic T cells into the CNS of
402 $A20^{\Delta CNS\text{-}EC}$ mice, confirming its contribution to T-cell mediated autoimmunity.
403
404 In agreement with these observations, our results additionally showed that the day of active
405 EAE onset could be delayed when ICOSL was knocked down in CNS-ECs of wildtype mice. As
406 transmigration of immune cells through the BBB precedes the development of EAE symptoms
407 (74,75), our data suggests that the delayed disease development is due to an impairment of T
408 cell adhesion to the BBB. The phenotype we observed is in accordance with EAE data from
409 mice in which other cell adhesion molecules (ICAM-1, ICAM-2, VCAM-1) were targeted
410 (36,76). Targeting of CNS microvascular EC-ICOSL thus seems to be an attractive approach for
411 controlling infiltration of pathogenic immune cells in the context of autoimmune
412 neuroinflammation. However, ICOSL is well-known to also function as co-stimulatory
413 molecule in an immunological context (77-79) and earlier studies targeting ICOS indicated a
414 protective effect of ICOS-ICOSL interaction in the priming phase of EAE (80,81). Thus, anti-
415 ICOSL treatment for CNS autoimmunity needs to be carefully evaluated as the desired effect
416 strongly relies on cell specificity as well as the time point of therapy.
417
418 In conclusion, our study sheds new light on two important aspects in the pathology of CNS
419 inflammation. Firstly, our data demonstrates a protective role for CNS endothelial A20 by
420 preventing the excessive expression of cell adhesion molecules and thus regulating the
421 infiltration of immune cells into the CNS. Secondly, we discovered ICOSL as an A20-regulated
422 cell adhesion molecule mediating the firm adhesion of Th1 and Th17 cells to the BBB. Overall,

this study suggests ICOSL as a potential therapeutic target in the treatment of CNS autoimmune diseases such as MS.

METHODS

Mice

All mice used were on the C57BL/6 background and housed under specific pathogen-free conditions. $A20^{fl/fl}$ mice (82) were crossed to Slco1c1-$CreER^{T2}$ mice (32) ($A20^{\Delta CNS\text{-}EC}$) and used for A20 western blot analysis, immunofluorescent stainings of brain vessels with collagen IV, CD31, occludin and VCAM-1, MCAO and active EAE in facility 2. For all other experiments analyzing $A20^{\Delta CNS\text{-}EC}$ mice, $A20^{fl/fl}$ mice (42) were crossed to Slco1c1-$CreER^{T2}$ mice (32). For generation of $A20^{\Delta EC}$ mice, $A20^{fl/fl}$ mice (42) were crossed to Cdh5(PAC)-$CreER^{T2}$ (33) mice. Cre-negative $A20^{fl/fl}$ littermates were used as controls. For sequencing experiments, $A20^{\Delta CNS\text{-}EC}$ mice were crossed to R26R-EYFP reporter mice (83). For AT-EAE experiments, Ly5.1 mice (B6.SJL-PtprcaPepcb/BoyCrl) were used as donor mice.

Tamoxifen treatment

A 20 mg/ml tamoxifen (Sigma-Aldrich) solution was prepared by suspension in olive oil (Sigma-Aldrich) containing 5 % ethanol. Tamoxifen was dissolved by rotation overnight at 4°C. Mice were injected intraperitoneally (i.p.) with 100 µl (= 2 mg tamoxifen) at five (for Slco1c1-$CreER^{T2}$ strains) or three (for Cdh5(PAC)-$CreER^{T2}$ strains) consecutive days at the age of 6-7 weeks and mice were used for experiments 2-4 weeks thereafter, unless otherwise indicated. $A20^{fl/fl}$ littermate controls were treated equally.

Active EAE induction

447 An emulsion of MOG_{35-55} in CFA was prepared by mixing 1 mg/ml MOG_{35-55} (GenScript) in PBS
448 with Complete Freund's Adjuvants (CFA, BD Biosciences) supplemented with *mycobacterium*
449 *tuberculosis* H37RA (BD Biosciences). 50 μg MOG_{35-55}/CFA were injected subcutaneously into
450 the tail base. At the day of immunization and two days later, 150 ng pertussis toxin (PTx, List
451 Biological Laboratories) in PBS were applied i.p. unless otherwise stated. For active EAE
452 induction in facility 2 (Supplemental Figure 1E-H) mice were immunized with an immunizing
453 emulsion (EK-2110, Hooke Laboratories) containing a $MOG_{35–55}$ peptide in Freund's adjuvant
454 as described before (84). Additionally, mice were treated with 400 ng PTx i.p. on the day of
455 immunization and one day later.
456 Mice were weighed daily and clinical scores were documented as follows: 0, no disease; 0.5:
457 limb tail; 1: paralyzed tail; 1.5: weakened righting reflex; 2: no righting reflex; 3: partial
458 paralysis of hind legs; 3.5: paralysis of one hind leg; 4: paralysis of both hind legs.
459
460 *Adoptive transfer (AT) EAE induction*
461 Ly5.1 mice were immunized with MOG/CFA and PTx as described above. Ten days after
462 immunization, spleen, inguinal and paraaortic lymph nodes were harvested and single-cell
463 suspensions were prepared and cultured in vitro in the presence of MOG_{35-55} peptide (20
464 μg/ml), anti-IFNγ (10 μg/ml; BioXCell), and IL-23 (15 ng/ml; Miltenyi Biotec). After 4 days, cells
465 were harvested and examined for blasting lymphocytes, as based on forward and side scatter
466 properties in flow cytometry. Cell suspensions were adjusted to 50×10^6 blasting cells/ml, and
467 100 μl of this suspension was injected intravenously (i.v.) into the tail veins of recipient mice,
468 accompanied by i.p. injections of PTx (150 ng) at the same day and 2 days later. Mice were
469 weighed daily and the clinical scores were assessed according to the scoring system described
470 above.

Permanent occlusion of the middle cerebral artery (MCAO)

The ischemic stroke model was performed as described before (85). Briefly, mice were anaesthetized using tribromoethanol (2.5%, 15µl/g body weight, i.p.). After a skin incision and removal of the left temporal muscle, a burr hole was drilled through which the stem of the middle cerebral artery was occluded by electrocoagulation (Model ICC50, Erbe). After suturing, mice were placed under a heating lamp until they fully recovered. After 48h, mice were perfused intracardially under deep anesthesia and brains were removed. Coronal cryosections were cut every 400 µm and stained using a silver technique (86). Infarcted areas were measured using ImageJ and infarct volume, edema, and edema-corrected infarct volume were calculated as described before (86).

Immunofluorescence staining

Immunoflurescence stainings were performed on fixed frozen sections of 10-20 µm. Primary antibodies against CD3ε (145-2C11, Armenian hamster monoclonal, eBioscience™, Thermo Fisher Scientific, 1:100), NeuN (1B7, Mouse monoclonal, Invitrogen Thermo Fisher Scientific, 1:500), CD31 (rabbit polyclonal, abcam, 1:100 or MEC 13.3, rat monoclonal, BD Pharmingen™, 1:500), laminin 1+2 (rabbit polyclonal, abcam, 1:500), collagen IV (rabbit polyclonal, abcam, 1:1000), occludin (rabbit polyclonal, Proteintech, 1:1000) and VCAM-1 (MVCAM.A, rat monoclonal, BD Pharmingen™, 1:1000) were incubated over night at 4°C. Sections were washed and secondary antibodies against rabbit IgG (CF488A, Sigma-Aldrich, 1:800 or CF™ 555, Sigma-Aldrich, 1:800 or Cy3, Jackson ImmunoResearch Labs, 1:400), Armenian hamster (Alexa Fluor 647, Jackson ImmunoResearch Labs, 1:800), mouse IgG (CF™ 647, Sigma-Aldrich, 1:500) or rat IgG (Alexa 488, Thermo Fisher Scientific, 1:400) were added for 45 min - 1.5 h at

room temperature. Afterwards, sections were mounted with DAPI Fluoromount-G® Mounting Medium (SouthernBiotech) or Mowiol 4-88 (Carl Roth) and images were acquired at a TCS SP8 inverse confocal microscope (Leica) or a DMI 6000B fluorescence microscope (Leica). Images were analyzed with ImageJ software as described before (22).

Culture of primary murine brain microvascular endothelial cells (pMBMEC)

Cortices from 8-12-week-old wildtype mice were used for pMBMEC isolation as described previously (87). Cells were seeded on 48-well culture dishes coated with Matrigel (ECM Gel from Engelbreth-Holm-Swarm murine sarcoma, supplied by Sigma-Aldrich). Culture medium was supplemented with 20% FCS, 2% non-essential amino acids and 5 µg/ml gentamicin. 1 ng/ml human fibroblast growth factor (FGF) (Sigma-Aldrich) and 4 µg/ml puromycin (Gibco) were added for the first 48 h of culture. Afterwards, the medium was changed to puromycin-free medium supplemented with FGF and was changed every other day.

Leukocyte cell isolation from CNS for flow cytometry

CNS tissue was dissected from mice transcardially perfused with 0.9% NaCl solution (Sigma-Aldrich) and digested with 2 mg/ml collagenase II (Gibco) and 25 µg/ml DNase I (Roche) for 20 min at 37 °C and subsequently homogenized with a 18-G needle. Cells were then separated using a 70–37–30% Percoll (Sigma-Aldrich) gradient centrifugation for 40 min, 500×*g* at 16 °C. Cells at the 70/37% interphase were carefully collected and washed in PBS/FCS prior to 10 min centrifugation at 500×*g*. To characterize MOG-specific T cells and cytokine production, cells were plated in 96-well U-bottom plates and re-activated with 20 µg/ml MOG_{35-55} peptide in the presence of brefeldin A (Sigma-Aldrich) in T cell medium for 6 h at 37 °C. Afterwards, cells were harvested and stained for flow cytometry analysis.

519

520 *Endothelial cell isolation for flow cytometry*

521 For CNS EC-isolation, mice were sacrificed and transcardially perfused as described above. The
522 dissected CNS tissue was digested with 2 mg/ml papain (Sigma-Aldrich) solution containing 25
523 µg/ml DNase I (Roche) for 30 min at 37 °C. During incubation, tissue was mechanically
524 homogenized using the gentleMACS™ Dissociator (Miltenyi). The resulting cell suspension was
525 filtered through a 70 µm cell strainer and centrifuged with a 22 % Percoll gradient for 30 min,
526 300×*g* at 15 °C. The pellet was used for flow cytometry staining.

527

528 *Flow cytometry analysis*

529 Before antibody staining, Fc receptors were blocked for 20 min using Fc-block (5 µg/ml)
530 (BioXCell). Single cell suspensions were stained for 30 min at 4 °C with antibodies against CD4
531 PerCP (GK1.5, rat monoclonal, 1:500, BioLegend), CD45 BV510 (30-F11, rat monoclonal, 1:200,
532 BioLegend), CD45.1 FITC (A20, mouse monoclonal, 1:1000, BioLegend), CD11b PECy7 (M1/70,
533 rat monoclonal, 1:1000, eBioscience™), Ly6C V450 (AL-21, rat monoclonal, 1:300 BD
534 Bioscience), Ly6C PerCP (HK1.4, rat monoclonal, 1:100, BioLegend), Ly6G PE (1A8, rat
535 monoclonal, 1:1000, BioLegend), CD11c APC (HL3, rat monoclonal, 1:800 BD Bioscience), CD19
536 PerCP (6D5, rat monoclonal, 1:400, BioLegend), TCRβ APC (H57-597, rat monoclonal, 1:1000,
537 BioLegend), CD31 PE (MEC 13.3, rat monoclonal, 1:100, BioLegend), CD31 PerCP-Cy5.5 (390,
538 rat monoclonal, 1:100, BioLegend), ICAM-1 APC (YN1/1.7.4, rat monoclonal, 1:300,
539 BioLegend), VCAM-1 PE-Cy7 (429 (MVCAM.A), rat monoclonal, 1:500, BioLegend), ICOSL
540 (CD275) PE (HK5.3, rat monoclonal, 1:100, BioLegend).

541 Afterwards, where indicated, cells were fixed and permeabilized with Cytofix/Cytoperm (BD
542 Bioscience) or Foxp3/Transcription Factor Staining Buffer Set (eBioscience™) and stained

543 overnight at 4 °C with intracellular antibodies. To specifically gate on MOG-specific cells, cells
544 were stained with anti-CD154 (CD40L) APC (MR1, hamster monoclonal, 1:200, BioLegend) and
545 cytokine production was assessed by staining with IL-17A eFl450 (eBio17B7, rat monoclonal,
546 1:300, eBioscience™), IFN-y PE-Cy7 (XMG1.2, rat monoclonal, 1:1000, eBioscience™) and
547 GM-CSF PE (MP1-22E9, rat monoclonal, 1:200, eBioscience™). Staining for Foxp3 was
548 performed with Foxp3-FITC (FJK-16s, rat monoclonal, 1:200, eBioscience™).
549 Cells were acquired with a FACSCanto II cytometer (BD Bioscience) using FACS Diva software
550 (BD Bioscience). Flow cytometry data was analyzed with FlowJo™ software version 10 (BD
551 Bioscience). For all analyses, doublets (FSC and SSC properties) and dead cells (dye inclusion,
552 fixable viability dye APC-ef780 eBioscience™) were excluded.
553
554 *Fluorescence activated cell sorting (FACS) of CNS-ECs*
555 Endothelial cells from the spinal cord were isolated and subsequently stained with a surface
556 marker antibody panel and directly acquired at a FACSAria III (BD Bioscience) with a 100 μm
557 nozzle.
558
559 *RNA isolation and RNA sequencing*
560 For RNA sequencing 500 cells were sorted into lysis buffer and full-length cDNA was
561 synthesized using the SMART-Seq® v4 Ultra® Low Input Kit (Takarabio). 1 ng of the resulting
562 cDNA was used for library preparation (Illumina Nextera XT DNA Library Prep Kit) according to
563 the manufacturer's instructions. Quantity was assessed using Invitrogen's Qubit HS assay kit
564 and library size was determined using Agilent's 2100 Bioanalyzer HS DNA assay. Barcoded
565 RNA-Seq libraries were onboard clustered using HiSeq® Rapid SR Cluster Kit v2 using 8pM and
566 59bps and were sequenced on the Illumina HiSeq2500 using HiSeq® Rapid SBS Kit v2 (59 Cycle).

The raw output data of the HiSeq was preprocessed according to the Illumina standard protocol.

RNA sequencing data analysis

Quality control on the sequencing data was performed with the FastQC tool (version 0.11.8, https://www.bioinformatics.babraham.ac.uk/projects/fastqc/). RNA sequencing reads were aligned to the ENSEMBL Mus_musculus.GRCm38 reference genome. The corresponding annotation (ENSEMBL v76) was retrieved from ENSEMBL FTP website. The STAR aligner (version 2.6.1a) was used to perform mapping to the reference genome. Alignments were processed with the featureCounts function of the Rsubread package (version 2.10.0), using the annotation file also used for supporting the alignment. The exploration, modeling, and interpretation of the expression data followed the protocols defined by Ludt *et. al* (2022) (88). Exploratory data analysis was performed with the pcaExplorer package (version 2.22.0). Differential expression analysis was performed with DESeq2 package (version 1.36.0), setting the false discovery rate (FDR) cutoff to 0.05. Accurate estimation of the effect sizes (described as log2 fold change) was performed using the apeglm shrinkage estimator (version 1.18.0). Gene expression profiles were plotted as heatmaps (color-coded standardized z-scores for the expression values, after regularized logarithm transformation) to enable comparison across samples, created with the GeneTonic package (version 2.0.3) (89). For functional annotation of Gene Ontology (GO) and analysis of KEGG pathway enrichment, the web-based DAVID 2021 tool was used.

FITC-dextran permeability assay

FITC-dextran (avg. mol. weight 3,000-5,000 Da, Sigma-Aldrich) was dissolved at 2 mM in PBS. 100 µl of this stock solution was injected i.p. into the mice. After 15 min, mice were sacrificed and perfused with 0.9% NaCl solution. Spinal cords and half brains were weighed and subsequently homogenized in 200 µl (spinal cord) or 500 µl (half brain) PBS in metal bead lysing matrix tubes (MP Biomedicals) using the FastPrep-24™ (MP Biomedicals) system. Tubes were centrifuged at 15,000 x g for 20 min at 4°C and 100 µl of the supernatant were transferred into a 96 well flat black plate (Greiner). FITC fluorescence was measured with a Spark plate reader (Tecan) with an excitation of 490/10 nm and an emission of 520/10 nm and raw fluorescence units (RFU) were normalized to tissue weights.

RNA isolation from pMBMECs and real time (RT) PCR

Isolation of RNA from cultured pMBMECs was performed with the ReliaPrep™ RNA Cell Miniprep System (Promega) following manufacturers guidelines. RNA concentrations were determined by measuring absorbance using the NanoQuant Plate™ (Tecan) at an Infinite M200 pro plate reader (Tecan). cDNA was synthesized using 200–1000 ng of total RNA with the QuantiTect® Reverse Transcription Kit (Qiagen) and subsequently used for qPCR, which was performed with the StepOnePlus™ Real-Time PCR System (Life Technologies) using SYBR Green reagent (Promega). Fold enrichment was calculated using the Delta–Delta CT method normalized to hypoxanthin-guanin-phosphoribosyltransferase (*Hprt*) as house-keeping reference. *Tnfaip3* primer were ordered as QuantiTect Primer Assay (QT00134064, Qiagen). *Icosl* primer (forward: 5'- AGGCTCCCTTGGACATCTCG -3'; reverse: 5'-CAGTACAGCAAGGACGGGGA -3') were self-designed using primer-BLAST tool from the National Center for Biotechnology Information (NCBI) and were synthesized by Metabion.

Western blot

Western blotting for the A20 protein was performed on primary brain endothelial cells of $A20^{fl/fl}$ and $A20^{\Delta CNS\text{-}EC}$ mice. After reaching confluence, cells were lysed and western blotting was performed as described before (22) using antibodies targeting A20 (A-12, mouse monoclonal, Santa Cruz, 1:500) and actin (C-11, goat polyclonal, Santa Cruz, 1:1000) and secondary antibodies against mouse IgG (HRP-coupled, Santa Cruz, 1:1000) and goat IgG (HRP-coupled, DAKO, 1:10000), respectively.

In vitro T cell static adhesion assay

pMBMECs were isolated and cultured as described above for 7 days on µ-dishes (ibidi GmbH). After 4 days, cells were stimulated with 20 ng/ml IL-1β for 72 h. Th1 or Th17 cells from 2D2 C57BL/6 mice were thawed and rested for approximately 4 h in T cell medium and subsequently labelled with 1 µM CellTracker™ Green (Thermo Fisher Scientific) for 30 min. pMBMECs were incubated with 15 µg/ml anti-mouse ICOSL (HK5.3, rat IgG2a monoclonal, BioXCell) or 15 µg/ml negative control (MJ7/18, rat IgG2a anti mouse endoglin (76)) for 30 min. 100,000 T cells were added to the pMBMECs and were allowed to adhere for 30 min on a shaking platform. Wells were washed with PBS and fixed with 1% PFA for 10 min before mounting on glass slides with DAPI. Images were acquired at an Eclipse E600 microscope (Nikon) and adhering T cells were counted using ImageJ software (National Institute of Health).

In vitro T cell migration assay under physiological flow

In vitro live-cell imaging of T cell diapedesis across pMBMECs was performed as described before (90). In brief, pMBMECs were isolated and cultured for 7 days on µ-dishes (ibidi GmbH). After 4 days, cells were stimulated with 20 ng/mL IL-1β for 72 h. 2D2 Th1 cells were resuspended at 1×10^6cells/ml in T cell medium. Prior to the experiment, pMBMECs were

treated with 15 μg/ml anti-mouse ICOSL (HK5.3, rat IgG2a monoclonal, BioXCell) or 15 μg/ml negative control (MJ7/18, rat IgG2a anti mouse endoglin (76)) for 30 min at 37°C. Accumulation of 2D2 Th1 on pMBMECs in the flow chamber was allowed for 4 min at a low shear (0.1 dyn/cm^2), followed by physiological shear (1.5 dyn/cm^2) for an additional 20 min, for a total recording time of 24 min. Image acquisition was performed at 10× magnification with the AxioObserver inverted microscope (Carl Zeiss) with differential interference contrast using the camera Evolve Delta (Teledyne Photometrics). Image frames were recorded every 10 s. Image analysis was performed using ImageJ software (National Institute of Health). T cell post-arrest behavior was defined and expressed as described previously (91). T cell crawling tracks were evaluated after manual tracking of individual T cells using the manual tracking plug-in of ImageJ. Distance and speed of crawling tracks were evaluated using chemotaxis and migration tool (version 2.0, Ibidi GmbH).

Adeno-associated virus (AAV) design and applications

For knockdown of ICOSL specifically in CNS-ECs AAV-BR1 (45) was used to deliver a short hairpin (sh) RNA against *Icosl* carrying the sense sequence GCAGAAAGTTTCACTGGAAATCTC to the target cells. The AAV-BR1-RSV-GFP-H1-shRNA_Icosl and the control AAV-BR1-RSV-GFP-H1-shRNA_scrambled constructs were produced by the Viral Vector Production Unit of the Universitat Autònoma Barcelona, Spain. The AAVs were delivered to us ready for use.

For in vitro experiments, pMBMECs grown in 48-well plates were transfected with 0.6x10^6 genomic particles (gp) per well four days after seeding. For in vivo experiments, constructs were delivered i.v. at a concentration of 1.8x10^{11} gp in 100 μl sterile PBS. AAV-BR1-eGFP was used as described elsewhere (45).

Statistics

Statistical analyses were performed with Prism v9 software (GraphPad). All values are represented as mean ± standard error of the mean (SEM) unless otherwise stated. *P* values were considered significant with $p<0.05$.

Study approval

All animal experiments were approved by the local administrations (Landesuntersuchungsamt Koblenz, Germany; Ministerium für Energiewende, Landwirtschaft, Umwelt und ländliche Räume, Kiel, Germany; individual approval numbers G20-1-049 and G22-1-005). Experiments were performed in accordance with the guidelines from the translational animal research center (TARC) Mainz, Germany. All efforts were made to minimize suffering of the mice.

Data availability

The RNA-seq data presented in this manuscript have been deposited in the Gene Expression Omnibus (GEO) under accession number GSE221318. All other data is available in the 'Supporting data values' file.

AUTHOR CONTRIBUTIONS

L.J. performed experiments, analyzed data, prepared figures, and wrote the manuscript. S.S., K.M., J.L., M.A.K., J.C.A., and J.W. performed experiments and analyzed data; F.M. performed bioinformatic analysis; N.R., I.P. and C.S. helped with experiments, data analysis and discussion. E.S. helped with experiments and manuscript writing. M.K. and T.B. provided reagents and guided preparation of samples for RNA seq. K.K. helped with histology and confocal imaging. M.H.H.S., D.S. and G.v.L. provided mouse strains. J.K. provided the AAV-BR1

plasmid. B.E. and M.S. were associated with conceptualization and supervision of the project, funding acquisition, and finalization of the manuscript. A.W. supervised the project, acquired funding and wrote the manuscript together with L.J.

ACKNOWLEDGEMENTS

We would like to thank Ralf Adams for allowing us to use the Cdh5-CreER^{T2} mice. We further thank Sara Barcos for excellent technical assistance and Dr. Natalia Soshnikova for helping with cDNA preparation for sequencing. We would like to thank Dr. Tommy Regen, Katlynn Carter, Rebecca Jasser, Elisa Blickberndt and Michaela Blanfeld for helping with the experiments. Work was supported by the computing infrastructure provided by the Core Facility Bioinformatics and the Core Facility Flow Cytometry (CFFC) at the University Medical Center Mainz. Graphical abstract was created with BioRender.com.

This work was funded by the Deutsche Forschungsgemeinschaft (DFG, German Research Foundation) project number 318346496 – SFB1292/2 to F.M., T.B., A.W., and project number 490846870 – TRR355/1 to A.W. and T.B. and SCHW 416/5-3 to M.S. This work was further funded with an unrestricted grant from Roche Global Neuroscience, Basel, Switzerland.

REFERENCES

1. Multiple-Sclerosis-International-Federation. The Atlas of MS. 2022. https://www.msif.org/news/2021/04/27/the-atlas-of-ms-part-2-goes-live/
2. Baecher-Allan C, et al. Multiple Sclerosis: Mechanisms and Immunotherapy. *Neuron*. Feb 21 2018;97(4):742-768. doi:10.1016/j.neuron.2018.01.021
3. Lassmann H. Multiple Sclerosis Pathology. *Cold Spring Harb Perspect Med*. Mar 1 2018;8(3)doi:10.1101/cshperspect.a028936
4. Waisman A, Johann L. Antigen-presenting cell diversity for T cell reactivation in central nervous system autoimmunity. *J Mol Med (Berl)*. Dec 2018;96(12):1279-1292. doi:10.1007/s00109-018-1709-7
5. Engelhardt B, et al. Vascular, glial, and lymphatic immune gateways of the central nervous system. *Acta Neuropathol*. Sep 2016;132(3):317-38. doi:10.1007/s00401-016-1606-5
6. Engelhardt B, Ransohoff RM. Capture, crawl, cross: the T cell code to breach the blood-brain barriers. *Trends Immunol*. Dec 2012;33(12):579-89. doi:10.1016/j.it.2012.07.004
7. Engelhardt B, et al. The movers and shapers in immune privilege of the CNS. *Nat Immunol*. Feb 2017;18(2):123-131. doi:10.1038/ni.3666
8. Lou J, et al. Direct cell/cell contact with stimulated T lymphocytes induces the expression of cell adhesion molecules and cytokines by human brain microvascular endothelial cells. *Eur J Immunol*. Dec 1996;26(12):3107-13. doi:10.1002/eji.1830261242
9. Carrithers MD, et al. Differential adhesion molecule requirements for immune surveillance and inflammatory recruitment. *Brain*. Jun 2000;123 (Pt 6):1092-101. doi:10.1093/brain/123.6.1092
10. Munji RN, et al. Profiling the mouse brain endothelial transcriptome in health and disease models reveals a core blood-brain barrier dysfunction module. *Nat Neurosci*. Nov 2019;22(11):1892-1902. doi:10.1038/s41593-019-0497-x
11. Profaci CP, et al. The blood-brain barrier in health and disease: Important unanswered questions. *J Exp Med*. Apr 6 2020;217(4)doi:10.1084/jem.20190062
12. Jeong HW, et al. Single-cell transcriptomics reveals functionally specialized vascular endothelium in brain. *Elife*. Oct 5 2022;11doi:10.7554/eLife.57520
13. Hauptmann J, et al. Interleukin-1 promotes autoimmune neuroinflammation by suppressing endothelial heme oxygenase-1 at the blood-brain barrier. *Acta Neuropathol*. Oct 2020;140(4):549-567. doi:10.1007/s00401-020-02187-x
14. Thornton P, et al. Interleukin-1 drives cerebrovascular inflammation via MAP kinase-independent pathways. *Curr Neurovasc Res*. Nov 2010;7(4):330-40. doi:10.2174/156720210793180800
15. Ledebur HC, Parks TP. Transcriptional regulation of the intercellular adhesion molecule-1 gene by inflammatory cytokines in human endothelial cells. Essential roles of a variant NF-kappa B site and p65 homodimers. *J Biol Chem*. Jan 13 1995;270(2):933-43. doi:10.1074/jbc.270.2.933
16. Wertheimer SJ, et al. Intercellular adhesion molecule-1 gene expression in human endothelial cells. Differential regulation by tumor necrosis factor-alpha and phorbol myristate acetate. *J Biol Chem*. Jun 15 1992;267(17):12030-5.
17. Neish AS, et al. Functional analysis of the human vascular cell adhesion molecule 1 promoter. *J Exp Med*. Dec 1 1992;176(6):1583-93. doi:10.1084/jem.176.6.1583

18. Shu HB, et al. Differential regulation of vascular cell adhesion molecule 1 gene expression by specific NF-kappa B subunits in endothelial and epithelial cells. *Mol Cell Biol*. Oct 1993;13(10):6283-9. doi:10.1128/mcb.13.10.6283-6289.1993
19. Tripathi AK, et al. Plasmodium falciparum-infected erythrocytes induce NF-kappaB regulated inflammatory pathways in human cerebral endothelium. *Blood*. Nov 5 2009;114(19):4243-52. doi:10.1182/blood-2009-06-226415
20. Jacob A, et al. C5a/CD88 signaling alters blood-brain barrier integrity in lupus through nuclear factor-kappaB. *J Neurochem*. Dec 2011;119(5):1041-51. doi:10.1111/j.1471-4159.2011.07490.x
21. Kielland A, et al. NF-kappaB activity in perinatal brain during infectious and hypoxic-ischemic insults revealed by a reporter mouse. *Brain Pathol*. Jul 2012;22(4):499-510. doi:10.1111/j.1750-3639.2011.00548.x
22. Ridder DA, et al. Brain endothelial TAK1 and NEMO safeguard the neurovascular unit. *J Exp Med*. Sep 21 2015;212(10):1529-49. doi:10.1084/jem.20150165
23. Opipari AW, Jr., et al. The A20 zinc finger protein protects cells from tumor necrosis factor cytotoxicity. *J Biol Chem*. Jun 25 1992;267(18):12424-7.
24. Cooper JT, et al. A20 blocks endothelial cell activation through a NF-kappaB-dependent mechanism. *J Biol Chem*. Jul 26 1996;271(30):18068-73. doi:10.1074/jbc.271.30.18068
25. Tewari M, et al. Lymphoid expression and regulation of A20, an inhibitor of programmed cell death. *J Immunol*. Feb 15 1995;154(4):1699-706.
26. International Multiple Sclerosis Genetics C, et al. Analysis of immune-related loci identifies 48 new susceptibility variants for multiple sclerosis. *Nat Genet*. Nov 2013;45(11):1353-60. doi:10.1038/ng.2770
27. Guedes RP, et al. A20 deficiency causes spontaneous neuroinflammation in mice. *J Neuroinflammation*. Jul 16 2014;11:122. doi:10.1186/1742-2094-11-122
28. Wang X, et al. Astrocytic A20 ameliorates experimental autoimmune encephalomyelitis by inhibiting NF-kappaB- and STAT1-dependent chemokine production in astrocytes. *Acta Neuropathol*. Nov 2013;126(5):711-724. doi:10.1007/s00401-013-1183-9
29. Voet S, et al. A20 critically controls microglia activation and inhibits inflammasome-dependent neuroinflammation. *Nat Commun*. May 23 2018;9(1):2036. doi:10.1038/s41467-018-04376-5
30. Mohebiany AN, et al. Microglial A20 Protects the Brain from CD8 T-Cell-Mediated Immunopathology. *Cell Rep*. Feb 4 2020;30(5):1585-1597 e6. doi:10.1016/j.celrep.2019.12.097
31. Zhang Y, et al. An RNA-sequencing transcriptome and splicing database of glia, neurons, and vascular cells of the cerebral cortex. *J Neurosci*. Sep 3 2014;34(36):11929-47. doi:10.1523/JNEUROSCI.1860-14.2014
32. Ridder DA, et al. TAK1 in brain endothelial cells mediates fever and lethargy. *J Exp Med*. Dec 19 2011;208(13):2615-23. doi:10.1084/jem.20110398
33. Wang Y, et al. Ephrin-B2 controls VEGF-induced angiogenesis and lymphangiogenesis. *Nature*. May 27 2010;465(7297):483-6. doi:10.1038/nature09002
34. Koutrolos M, et al. Treg cells mediate recovery from EAE by controlling effector T cell proliferation and motility in the CNS. *Acta Neuropathol Commun*. Dec 5 2014;2:163. doi:10.1186/s40478-014-0163-1
35. Brown WR. A review of string vessels or collapsed, empty basement membrane tubes. *J Alzheimers Dis*. 2010;21(3):725-39. doi:10.3233/JAD-2010-100219

798 36. Abadier M, et al. Cell surface levels of endothelial ICAM-1 influence the transcellular
799 or paracellular T-cell diapedesis across the blood-brain barrier. *Eur J Immunol*. Apr
800 2015;45(4):1043-58. doi:10.1002/eji.201445125
801 37. Polman CH, et al. A randomized, placebo-controlled trial of natalizumab for relapsing
802 multiple sclerosis. *N Engl J Med*. Mar 2 2006;354(9):899-910. doi:10.1056/NEJMoa044397
803 38. Rudick RA, et al. Natalizumab plus interferon beta-1a for relapsing multiple sclerosis.
804 *N Engl J Med*. Mar 2 2006;354(9):911-23. doi:10.1056/NEJMoa044396
805 39. Havrdova E, et al. Effect of natalizumab on clinical and radiological disease activity in
806 multiple sclerosis: a retrospective analysis of the Natalizumab Safety and Efficacy in
807 Relapsing-Remitting Multiple Sclerosis (AFFIRM) study. *Lancet Neurol*. Mar 2009;8(3):254-60.
808 doi:10.1016/S1474-4422(09)70021-3
809 40. Bloomgren G, et al. Risk of natalizumab-associated progressive multifocal
810 leukoencephalopathy. *N Engl J Med*. May 17 2012;366(20):1870-80.
811 doi:10.1056/NEJMoa1107829
812 41. Caravagna C, et al. Diversity of innate immune cell subsets across spatial and
813 temporal scales in an EAE mouse model. *Sci Rep*. Mar 23 2018;8(1):5146.
814 doi:10.1038/s41598-018-22872-y
815 42. Hovelmeyer N, et al. A20 deficiency in B cells enhances B-cell proliferation and results
816 in the development of autoantibodies. *Eur J Immunol*. Mar 2011;41(3):595-601.
817 doi:10.1002/eji.201041313
818 43. Khayyamian S, et al. ICOS-ligand, expressed on human endothelial cells, costimulates
819 Th1 and Th2 cytokine secretion by memory CD4+ T cells. *Proc Natl Acad Sci U S A*. Apr 30
820 2002;99(9):6198-203. doi:10.1073/pnas.092576699
821 44. Wheway J, et al. The brain microvascular endothelium supports T cell proliferation
822 and has potential for alloantigen presentation. *PLoS One*. 2013;8(1):e52586.
823 doi:10.1371/journal.pone.0052586
824 45. Korbelin J, et al. A brain microvasculature endothelial cell-specific viral vector with
825 the potential to treat neurovascular and neurological diseases. *EMBO Mol Med*. Jun
826 2016;8(6):609-25. doi:10.15252/emmm.201506078
827 46. Ansari AM, et al. Cellular GFP Toxicity and Immunogenicity: Potential Confounders in
828 in Vivo Cell Tracking Experiments. *Stem Cell Rev Rep*. Oct 2016;12(5):553-559.
829 doi:10.1007/s12015-016-9670-8
830 47. Barclay AN. Membrane proteins with immunoglobulin-like domains--a master
831 superfamily of interaction molecules. *Semin Immunol*. Aug 2003;15(4):215-23.
832 doi:10.1016/s1044-5323(03)00047-2
833 48. Lecuyer MA, et al. Dual role of ALCAM in neuroinflammation and blood-brain barrier
834 homeostasis. *Proc Natl Acad Sci U S A*. Jan 24 2017;114(4):E524-E533.
835 doi:10.1073/pnas.1614336114
836 49. Michel L, et al. Activated leukocyte cell adhesion molecule regulates B lymphocyte
837 migration across central nervous system barriers. *Sci Transl Med*. Nov 13
838 2019;11(518)doi:10.1126/scitranslmed.aaw0475
839 50. Larochelle C, et al. Melanoma cell adhesion molecule identifies encephalitogenic T
840 lymphocytes and promotes their recruitment to the central nervous system. *Brain*. Oct
841 2012;135(Pt 10):2906-24. doi:10.1093/brain/aws212
842 51. Larochelle C, et al. Melanoma cell adhesion molecule-positive CD8 T lymphocytes
843 mediate central nervous system inflammation. *Ann Neurol*. Jul 2015;78(1):39-53.
844 doi:10.1002/ana.24415

52. Charabati M, et al. DICAM promotes TH17 lymphocyte trafficking across the blood-brain barrier during autoimmune neuroinflammation. *Sci Transl Med*. Jan 5 2022;14(626):eabj0473. doi:10.1126/scitranslmed.abj0473
53. Du F, et al. Inflammatory Th17 Cells Express Integrin alphavbeta3 for Pathogenic Function. *Cell Rep*. Aug 2 2016;16(5):1339-1351. doi:10.1016/j.celrep.2016.06.065
54. Koh KH, et al. Nonimmune cell-derived ICOS ligand functions as a renoprotective alphavbeta3 integrin-selective antagonist. *J Clin Invest*. Apr 1 2019;129(4):1713-1726. doi:10.1172/JCI123386
55. Dopp JM, et al. Expression of ICAM-1, VCAM-1, L-selectin, and leukosialin in the mouse central nervous system during the induction and remission stages of experimental allergic encephalomyelitis. *J Neuroimmunol*. Oct 1994;54(1-2):129-44. doi:10.1016/0165-5728(94)90239-9
56. Lee SJ, Benveniste EN. Adhesion molecule expression and regulation on cells of the central nervous system. *J Neuroimmunol*. Aug 3 1999;98(2):77-88. doi:10.1016/s0165-5728(99)00084-3
57. Alvarez JI, et al. Disruption of central nervous system barriers in multiple sclerosis. *Biochim Biophys Acta*. Feb 2011;1812(2):252-64. doi:10.1016/j.bbadis.2010.06.017
58. Larochelle C, et al. How do immune cells overcome the blood-brain barrier in multiple sclerosis? *FEBS Lett*. Dec 1 2011;585(23):3770-80. doi:10.1016/j.febslet.2011.04.066
59. Merrill JE, Murphy SP. Inflammatory events at the blood brain barrier: regulation of adhesion molecules, cytokines, and chemokines by reactive nitrogen and oxygen species. *Brain Behav Immun*. Dec 1997;11(4):245-63. doi:10.1006/brbi.1997.0496
60. O'Carroll SJ, et al. Pro-inflammatory TNFalpha and IL-1beta differentially regulate the inflammatory phenotype of brain microvascular endothelial cells. *J Neuroinflammation*. Jul 8 2015;12:131. doi:10.1186/s12974-015-0346-0
61. Levesque SA, et al. Myeloid cell transmigration across the CNS vasculature triggers IL-1beta-driven neuroinflammation during autoimmune encephalomyelitis in mice. *J Exp Med*. May 30 2016;213(6):929-49. doi:10.1084/jem.20151437
62. Saitou M, et al. Occludin-deficient embryonic stem cells can differentiate into polarized epithelial cells bearing tight junctions. *J Cell Biol*. Apr 20 1998;141(2):397-408. doi:10.1083/jcb.141.2.397
63. Saitou M, et al. Complex phenotype of mice lacking occludin, a component of tight junction strands. *Mol Biol Cell*. Dec 2000;11(12):4131-42. doi:10.1091/mbc.11.12.4131
64. Yu AS, et al. Knockdown of occludin expression leads to diverse phenotypic alterations in epithelial cells. *Am J Physiol Cell Physiol*. Jun 2005;288(6):C1231-41. doi:10.1152/ajpcell.00581.2004
65. Schulzke JD, et al. Epithelial transport and barrier function in occludin-deficient mice. *Biochim Biophys Acta*. May 15 2005;1669(1):34-42. doi:10.1016/j.bbamem.2005.01.008
66. Daems CSMVVvLGDHRC-VZCP. A20/TNFAIP3 heterozygosity predisposes to behavioral symptoms in a mouse model for neuropsychiatric lupus. *Brain, Behavior, & Immunity - Health*. 2020;
67. Gelderblom M, et al. Neutralization of the IL-17 axis diminishes neutrophil invasion and protects from ischemic stroke. *Blood*. Nov 1 2012;120(18):3793-802. doi:10.1182/blood-2012-02-412726
68. Liesz A, et al. Inhibition of lymphocyte trafficking shields the brain against deleterious neuroinflammation after stroke. *Brain*. Mar 2011;134(Pt 3):704-20. doi:10.1093/brain/awr008

69. Neumann J, et al. Very-late-antigen-4 (VLA-4)-mediated brain invasion by neutrophils leads to interactions with microglia, increased ischemic injury and impaired behavior in experimental stroke. *Acta Neuropathol*. Feb 2015;129(2):259-77. doi:10.1007/s00401-014-1355-2
70. Lyck R, et al. ALCAM (CD166) is involved in extravasation of monocytes rather than T cells across the blood-brain barrier. *J Cereb Blood Flow Metab*. Aug 2017;37(8):2894-2909. doi:10.1177/0271678X16678639
71. Schneider-Hohendorf T, et al. VLA-4 blockade promotes differential routes into human CNS involving PSGL-1 rolling of T cells and MCAM-adhesion of TH17 cells. *J Exp Med*. Aug 25 2014;211(9):1833-46. doi:10.1084/jem.20140540
72. Charabati M, et al. MCAM+ brain endothelial cells contribute to neuroinflammation by recruiting pathogenic CD4+ T lymphocytes. *Brain*. Apr 19 2023;146(4):1483-1495. doi:10.1093/brain/awac389
73. Roussel L, et al. Loss of human ICOSL results in combined immunodeficiency. *J Exp Med*. Dec 3 2018;215(12):3151-3164. doi:10.1084/jem.20180668
74. Schlager C, et al. Effector T-cell trafficking between the leptomeninges and the cerebrospinal fluid. *Nature*. Feb 18 2016;530(7590):349-53. doi:10.1038/nature16939
75. Bartholomaus I, et al. Effector T cell interactions with meningeal vascular structures in nascent autoimmune CNS lesions. *Nature*. Nov 5 2009;462(7269):94-8. doi:10.1038/nature08478
76. Engelhardt B, et al. The development of experimental autoimmune encephalomyelitis in the mouse requires alpha4-integrin but not alpha4beta7-integrin. *J Clin Invest*. Dec 15 1998;102(12):2096-105. doi:10.1172/JCI4271
77. Dong C, et al. ICOS co-stimulatory receptor is essential for T-cell activation and function. *Nature*. Jan 4 2001;409(6816):97-101. doi:10.1038/35051100
78. Mak TW, et al. Costimulation through the inducible costimulator ligand is essential for both T helper and B cell functions in T cell-dependent B cell responses. *Nat Immunol*. Aug 2003;4(8):765-72. doi:10.1038/ni947
79. Coyle AJ, et al. The CD28-related molecule ICOS is required for effective T cell-dependent immune responses. *Immunity*. Jul 2000;13(1):95-105. doi:10.1016/s1074-7613(00)00011-x
80. Rottman JB, et al. The costimulatory molecule ICOS plays an important role in the immunopathogenesis of EAE. *Nat Immunol*. Jul 2001;2(7):605-11. doi:10.1038/89750
81. Galicia G, et al. ICOS deficiency results in exacerbated IL-17 mediated experimental autoimmune encephalomyelitis. *J Clin Immunol*. Jul 2009;29(4):426-33. doi:10.1007/s10875-009-9287-7
82. Vereecke L, et al. Enterocyte-specific A20 deficiency sensitizes to tumor necrosis factor-induced toxicity and experimental colitis. *J Exp Med*. Jul 5 2010;207(7):1513-23. doi:10.1084/jem.20092474
83. Srinivas S, et al. Cre reporter strains produced by targeted insertion of EYFP and ECFP into the ROSA26 locus. *BMC Dev Biol*. 2001;1:4. doi:10.1186/1471-213x-1-4
84. Chen H, et al. Hydroxycarboxylic acid receptor 2 mediates dimethyl fumarate's protective effect in EAE. *J Clin Invest*. May 2014;124(5):2188-92. doi:10.1172/JCI72151
85. Wenzel J, et al. Endogenous THBD (Thrombomodulin) Mediates Angiogenesis in the Ischemic Brain-Brief Report. *Arterioscler Thromb Vasc Biol*. Dec 2020;40(12):2837-2844. doi:10.1161/ATVBAHA.120.315061

86. Lubjuhn J, et al. Functional testing in a mouse stroke model induced by occlusion of the distal middle cerebral artery. *J Neurosci Methods*. Oct 30 2009;184(1):95-103. doi:10.1016/j.jneumeth.2009.07.029
87. Coisne C, et al. Mouse syngenic in vitro blood-brain barrier model: a new tool to examine inflammatory events in cerebral endothelium. *Lab Invest*. Jun 2005;85(6):734-46. doi:10.1038/labinvest.3700281
88. Ludt A, et al. Interactive and Reproducible Workflows for Exploring and Modeling RNA-seq Data with pcaExplorer, Ideal, and GeneTonic. *Curr Protoc*. Apr 2022;2(4):e411. doi:10.1002/cpz1.411
89. Marini F, et al. GeneTonic: an R/Bioconductor package for streamlining the interpretation of RNA-seq data. *BMC Bioinformatics*. Dec 23 2021;22(1):610. doi:10.1186/s12859-021-04461-5
90. Coisne C, et al. Live cell imaging techniques to study T cell trafficking across the blood-brain barrier in vitro and in vivo. *Fluids Barriers CNS*. Jan 21 2013;10(1):7. doi:10.1186/2045-8118-10-7
91. Marchetti L, et al. ACKR1 favors transcellular over paracellular T-cell diapedesis across the blood-brain barrier in neuroinflammation in vitro. *Eur J Immunol*. Jan 2022;52(1):161-177. doi:10.1002/eji.202149238

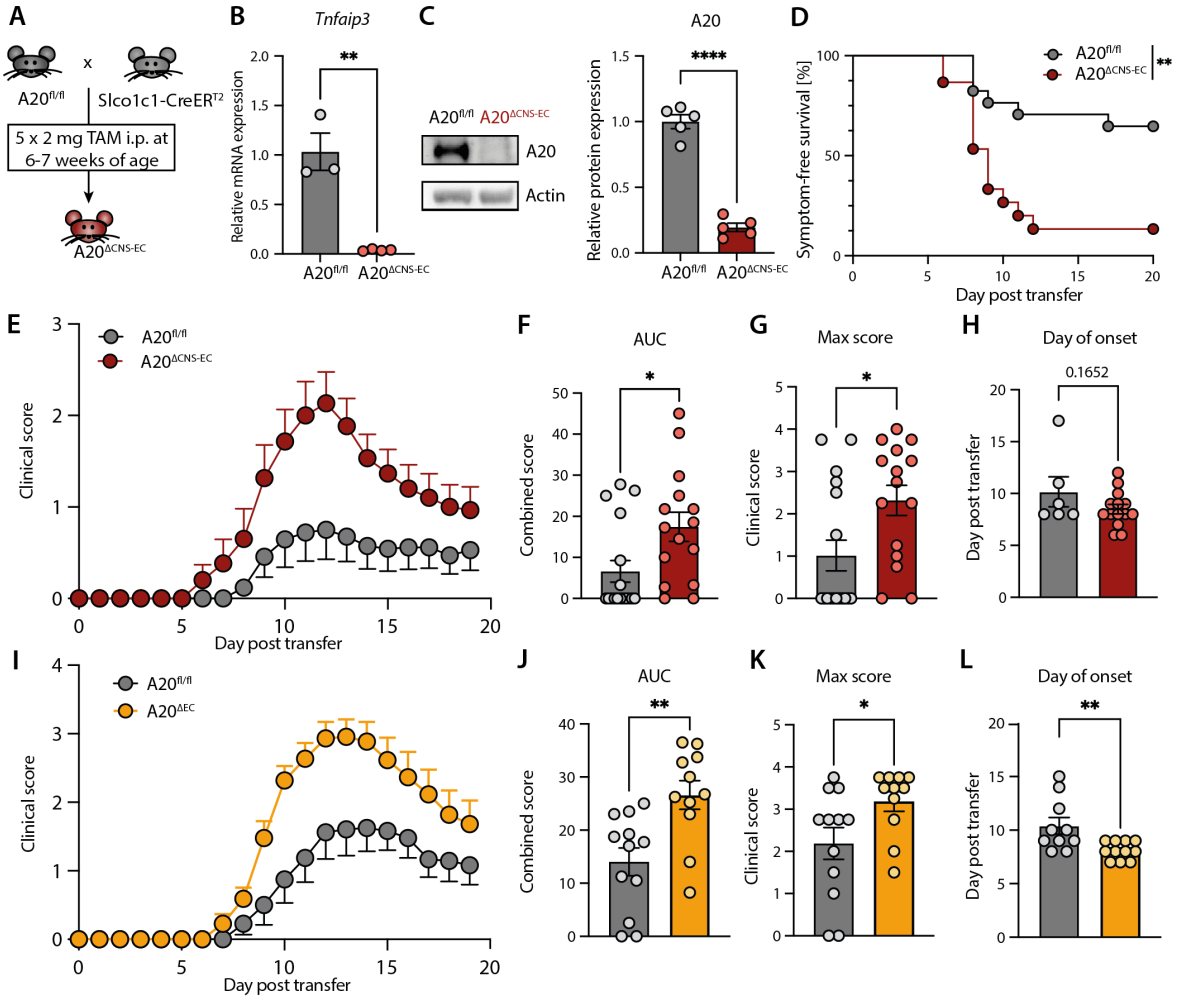

Figure 1: CNS EC-A20 plays a protective role in CNS autoimmunity

(A) Breeding strategy for generation of A20$^{\Delta CNS\text{-}EC}$ mice. Conditional deletion of *Tnfaip3* in A20$^{\Delta CNS\text{-}EC}$ mice is achieved through tamoxifen (TAM) injections. (B) Validation of *Tnfaip3* deletion in pMBMECs from A20$^{\Delta CNS\text{-}EC}$ mice by RT-PCR. *Tnfaip3* mRNA levels are presented relative to control (n = 3-4 mice per group). (C) Western blot analysis of A20 protein in cultured primary brain endothelial cells from A20$^{\Delta CNS\text{-}EC}$ and littermate control mice. Protein expression of A20 is normalized to actin levels and presented relative to the expression in controls (n = 5 mice per group). (D-H) Adoptive transfer (AT)-EAE disease in A20$^{\Delta CNS\text{-}EC}$ mice and A20$^{fl/fl}$ littermate. Clinical signs of EAE were monitored daily. Data is pooled from two independent experiments with n = 15-17 mice per group. (D) Probability of symptom-free survival is shown as Kaplan Meier curve. (E) Clinical signs of EAE are shown as mean clinical disease scores +/- SEM. (F) Area under the curve (AUC), (G) maximum clinical scores and (H) day of onset analyses of clinical course shown in (E). Every circle represents a single mouse. (I-L) AT-EAE disease was induced in A20$^{\Delta EC}$ lacking A20 in all endothelial cells driven by the Cdh5-CreER^{T2} and A20$^{fl/fl}$ littermate controls as described before. Clinical signs of EAE were monitored daily. Data is pooled from two independent experiments with n = 11-12 mice per group. (I) Clinical signs of EAE are shown as mean clinical disease scores +/- SEM. (J) AUC, (K) maximum clinical scores and (L) day of onset analyses of clinical course shown in (I). Every circle represents a single mouse. Statistical significance was determined by two-tailed unpaired Student's t-test (B, C, F-H, J-L) or Log-rank (Mantel-Cox) test (D). * p<0.05, ** p<0.01, **** p<0.0001.

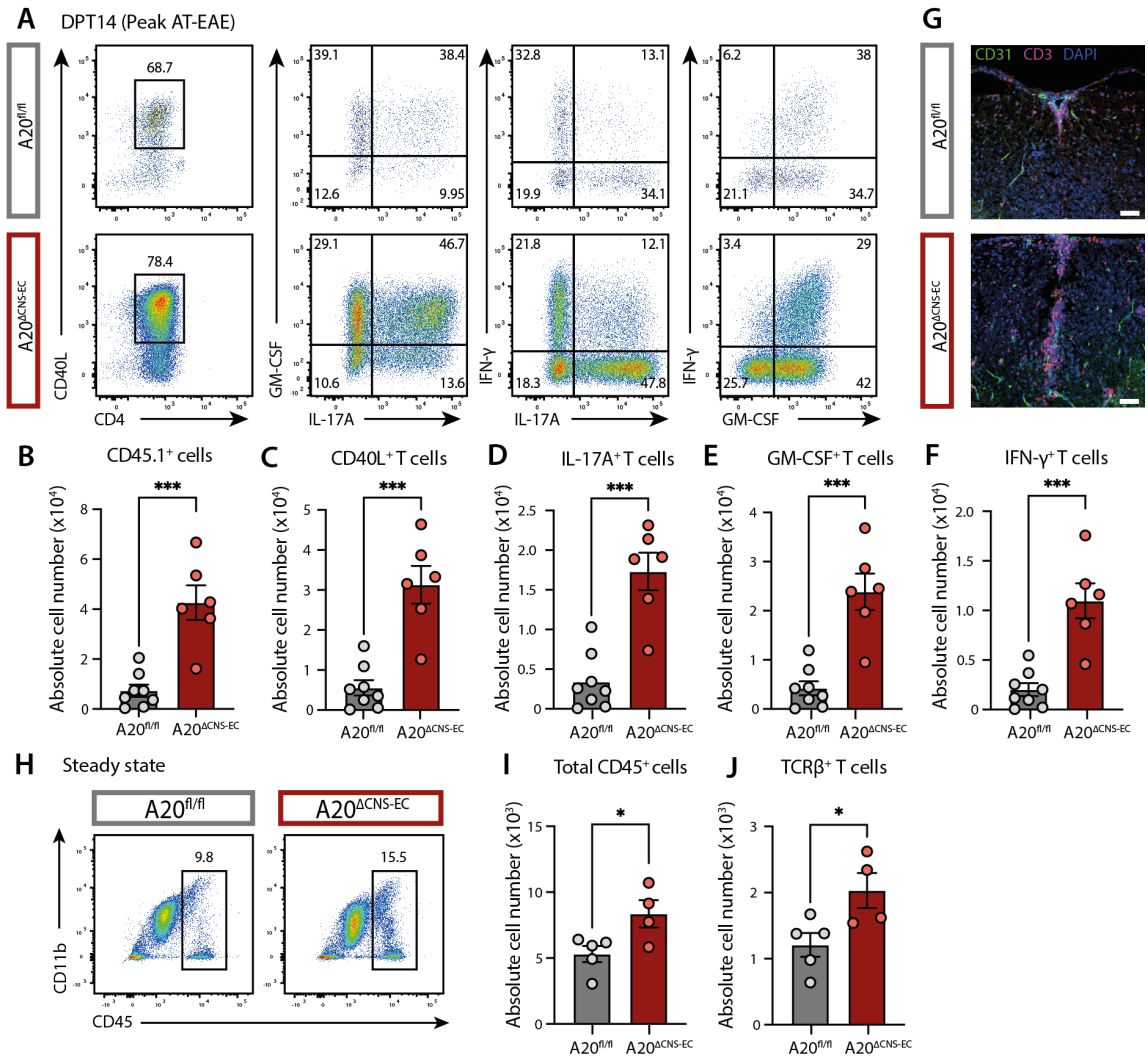

Figure 2: Loss of CNS EC-A20 drives T cell infiltration during EAE and in the steady state
(A-E) AT-EAE disease was induced in A20$^{\Delta CNS\text{-}EC}$ mice and A20$^{fl/fl}$ littermate controls. At the peak of the disease (day post transfer (DPT) 14) SC-infiltrating CD45.1$^+$ transferred T cells were isolated and analyzed by flow cytometry after a MOG recall assay *ex vivo*. (A) Representative gating strategy for CD40L$^+$ CD4$^+$ T cells and amongst them frequencies of GM-CSF, IL-17A, IFN-γ and double-producing cells; pre-gated as single, live, CD45.1$^+$ transferred T cells. (B-F) Quantification of immune cell populations. Data is representative for 2 independent experiments with n = 6-8 mice per group. (B) Absolute cell numbers of CD45.1$^+$ transferred T cells, (C) CD40L$^+$ among transferred T cells, (D) IL-17A$^+$, (E) GM-CSF$^+$ and (F) IFN-γ$^+$ cells amongst CD40L$^+$ cells. (G) Representative immunostainings of CD3$^+$ T cells (magenta), CD31$^+$ endothelial cells (green) and nuclear staining (DAPI, blue) in the SC at the peak of AT-EAE (DPT14) of A20$^{\Delta CNS\text{-}EC}$ and A20$^{fl/fl}$ mice (scale bar = 50 µm). (H-J) Flow cytometric analysis of CNS-infiltrating cells in the steady state of A20$^{\Delta CNS\text{-}EC}$ and A20$^{fl/fl}$ mice one week after TAM treatment. Cells were isolated from pooled SC and brain tissue. (H) Representative gating strategy for CD45$^+$ total immune cells; pre-gated as single, live cells. (I-J) Quantification of immune cell populations. Data is representative for 3 independent experiments with n = 4-5 mic per group. (I) Absolute cell numbers of CD45$^+$ total infiltrates and amongst them (J) number of TCRβ$^+$ T cells. Statistical significance was determined by two-tailed unpaired Student's t-test. * p<0.05, *** p<0.001.

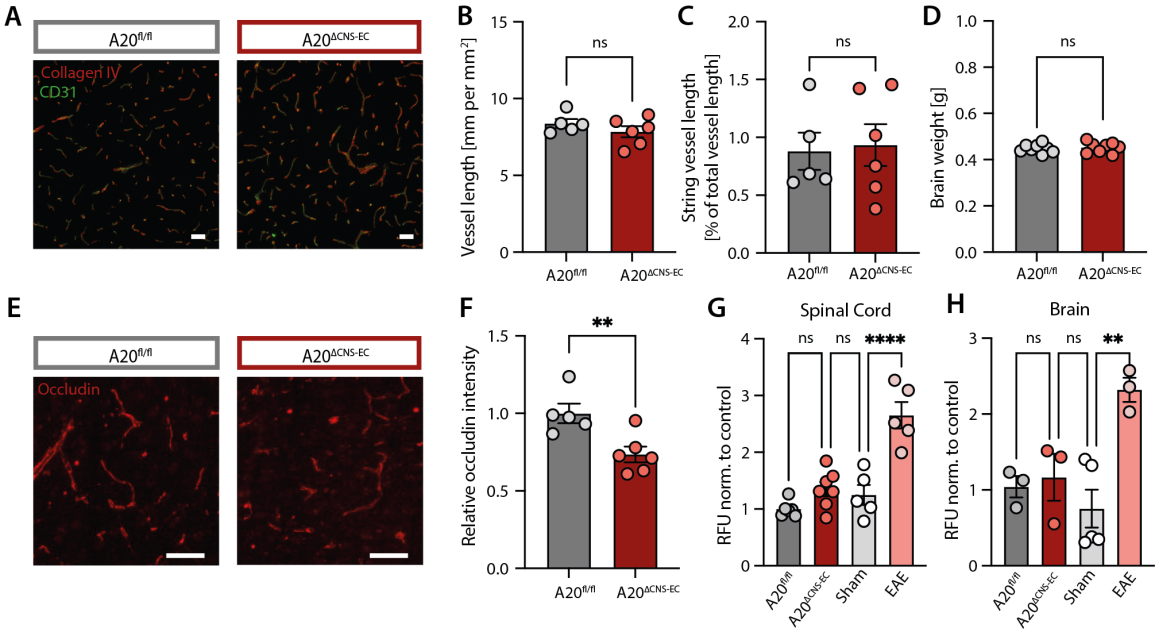

Figure 3: A20-deficiency in CNS-ECs does not impair BBB integrity

(A-C) Brain sections from $A20^{\Delta CNS\text{-}EC}$ and $A20^{fl/fl}$ mice were stained for collagen IV (red) and CD31 (green) to determine vessel length and string vessel length. String vessels were identified as capillaries that have lost CD31-positive endothelial cells and only consist of the basement membrane protein collagen IV. Representative microscopic images are shown in (A). Scale bar = 50 µm. (B) Vessel length in mm per mm^2 and (C) string vessel length [%] normalized to $A20^{fl/fl}$ littermate controls were quantified (n = 5-6 mice per group). (D) Brain weight of $A20^{\Delta CNS\text{-}EC}$ and $A20^{fl/fl}$ mice (n = 8 mice per group) shown as representative of 2 individual cohorts. (E-F) Brain sections from $A20^{\Delta CNS\text{-}EC}$ and $A20^{fl/fl}$ mice were stained for occludin (red). Representative microscopic images are shown in (E). Scale bar = 50 µm. (F) Occludin intensity was quantified and is presented relative to $A20^{fl/fl}$ littermate control mice (n = 5-6 mice per group) as representative of 2 individual cohorts. (G-H) $A20^{\Delta CNS\text{-}EC}$ and $A20^{fl/fl}$ mice were injected with 2 mM 3-5 kDa FITC-dextran in PBS i.p. After 15 minutes, SC and brain were isolated and homogenized in PBS. Fluorescence was measured in the supernatant and raw fluorescence units (RFU) were normalized to tissue weight. PBS injected mice were used as Sham controls; mice at the peak of an active EAE (scores between 1.5 – 3.5) were used as positive controls. Normalized RFUs are shown for SC (G) and brain (H) relative to $A20^{fl/fl}$ controls (SC: n = 5-7; brain: n = 3-5 mice per group). Statistical significance was determined by two-tailed unpaired Student's t-test (B-D, F) or ordinary one-way ANOVA with Tukey's multiple comparisons test (G, H). Ns = not significant, ** $p<0.01$, **** $p<0.0001$.

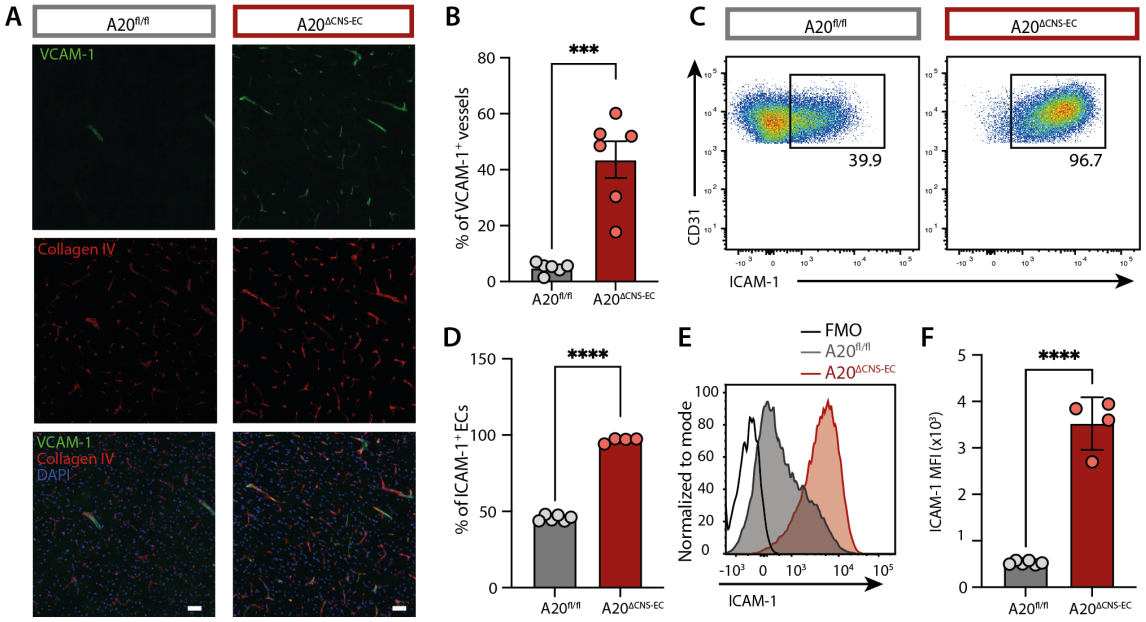

Figure 4: *A20-deficiency in CNS-ECs drives adhesion molecule expression*

(A-B) Brain sections were stained for VCAM-1 (green) and collagen IV (red) together with a nuclear staining (DAPI, blue). Representative microscopic images are shown in (A). Scale bar = 50 µm. (B) Frequency of VCAM-1$^+$ vessels quantified as percentage of all collagen IV positive vessels (n = 6 mice per group). (C-F) Flow cytometric analysis of ICAM-1 on CNS-ECs isolated from pooled brain and spinal cord tissue from A20$^{\Delta CNS\text{-}EC}$ and A20$^{fl/fl}$ littermate control mice. Data is representative from 3 individual experiments with n = 4-6 mice per group. (C) Representative gating strategy for ICAM-1$^+$ CNS-ECs; gate was set based on fluorescence minus one (FMO) control. CNS-ECs were pre-gated as single, live, CD45$^-$ CD11b$^-$ Ly6C$^+$ CD31$^+$ cells. (D) Frequency of ICAM-1$^+$ ECs quantified as percentage of all CNS-ECs. (E) Histogram of ICAM-1 fluorescence on ECs in A20$^{\Delta CNS\text{-}EC}$, A20$^{fl/fl}$ mice and FMO control. (F) Mean fluorescence intensity (MFI) presented as geometric mean of ICAM-1 on CNS-ECs. Statistical significance was determined by two-tailed unpaired Student's t-test (B, D, F). *** p<0.001, **** p<0.0001.

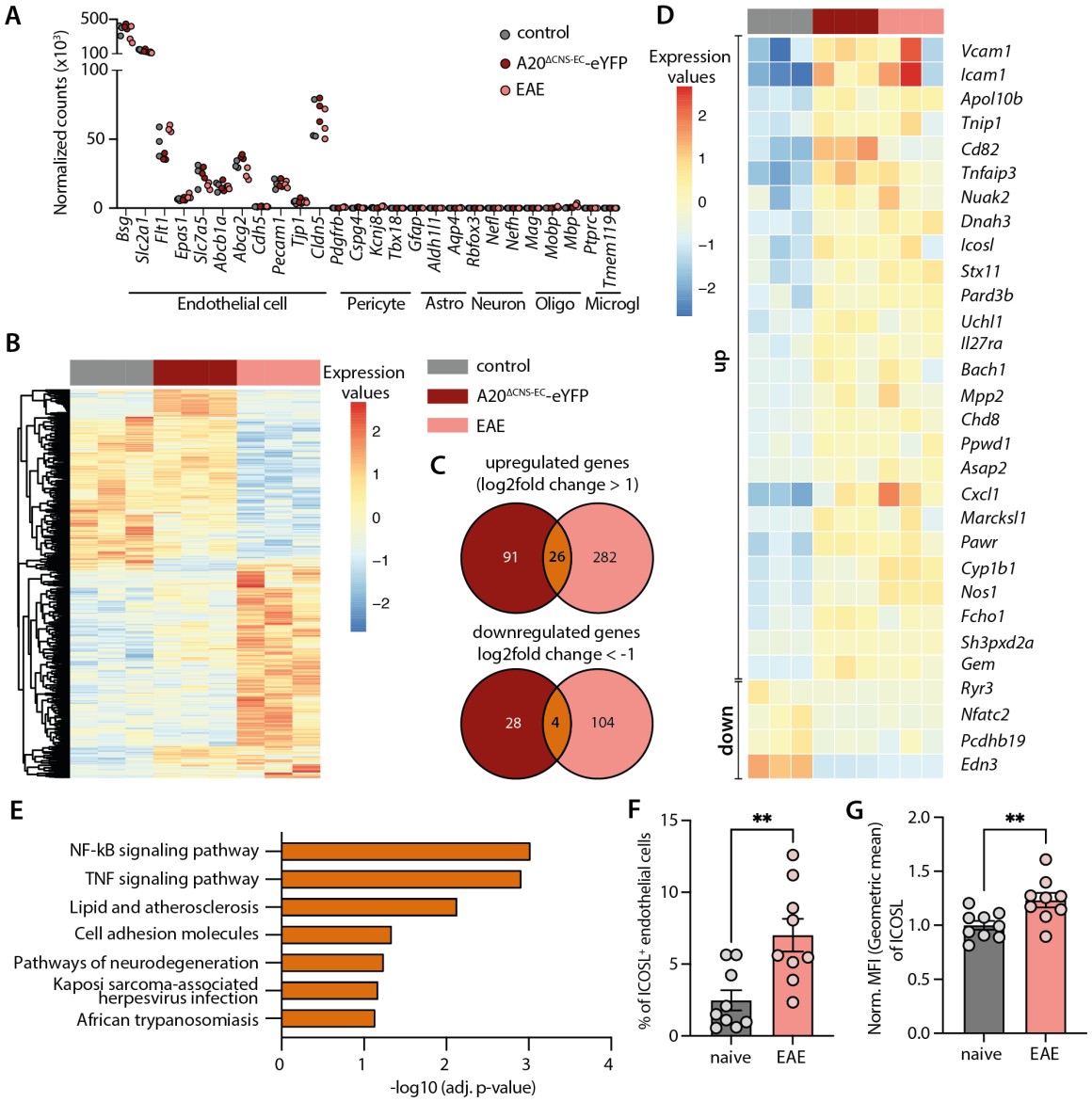

Figure 5: RNA sequencing identifies A20-regulated ICOSL as potential adhesion molecule

(A-E) RNA sequencing of sorted CNS-ECs from SC of naïve A20$^{\Delta CNS\text{-}EC}$-eYFP (red), A20$^{fl/fl}$ littermate control mice (referred to as control, grey), and A20$^{fl/fl}$ mice at day 10 after EAE immunization with MOG$_{35\text{-}55}$/CFA and PTx (referred to as EAE, pink) (n = 3 mice per group). (A) Purity of EC sorting was assessed by plotting normalized counts for marker genes of ECs, pericytes, astrocytes (astro), neurons, oligodendrocytes (oligo) and microglia (microgl). (B) Heatmap showing color-coded standardized z-scores for the expression values of genes differentially regulated in A20$^{\Delta CNS\text{-}EC}$ or EAE CNS-ECs compared to control. Each column represents an individual mouse. (C) Venn diagrams showing the number of commonly upregulated (log2fold change > 1) and commonly downregulated (log2fold change < -1) genes in A20$^{\Delta CNS\text{-}EC}$-eYFP and EAE mice compared to control as overlap of the circles. (D) Heatmap showing color-coded standardized z-scores for the expression values of the 30 commonly DE genes. Each column represents an individual mouse. (E) KEGG pathway analysis of the 30 commonly differentially expressed genes shown in (D). (F-G) ECs were isolated from the CNS of wildtype mice at day 10 post immunization with MOG$_{35\text{-}55}$/CFA and PTx or from naïve mice and stained for flow cytometric analysis of ICOSL. Data is pooled from 3 individual experiments with n = 9 mice per group. (F) Percentage and (G) normalized geometric MFI of ICOSL amongst

all ECs were quantified. Statistical significance was determined by two-tailed unpaired Student's t-test. ** $p<0.01$.

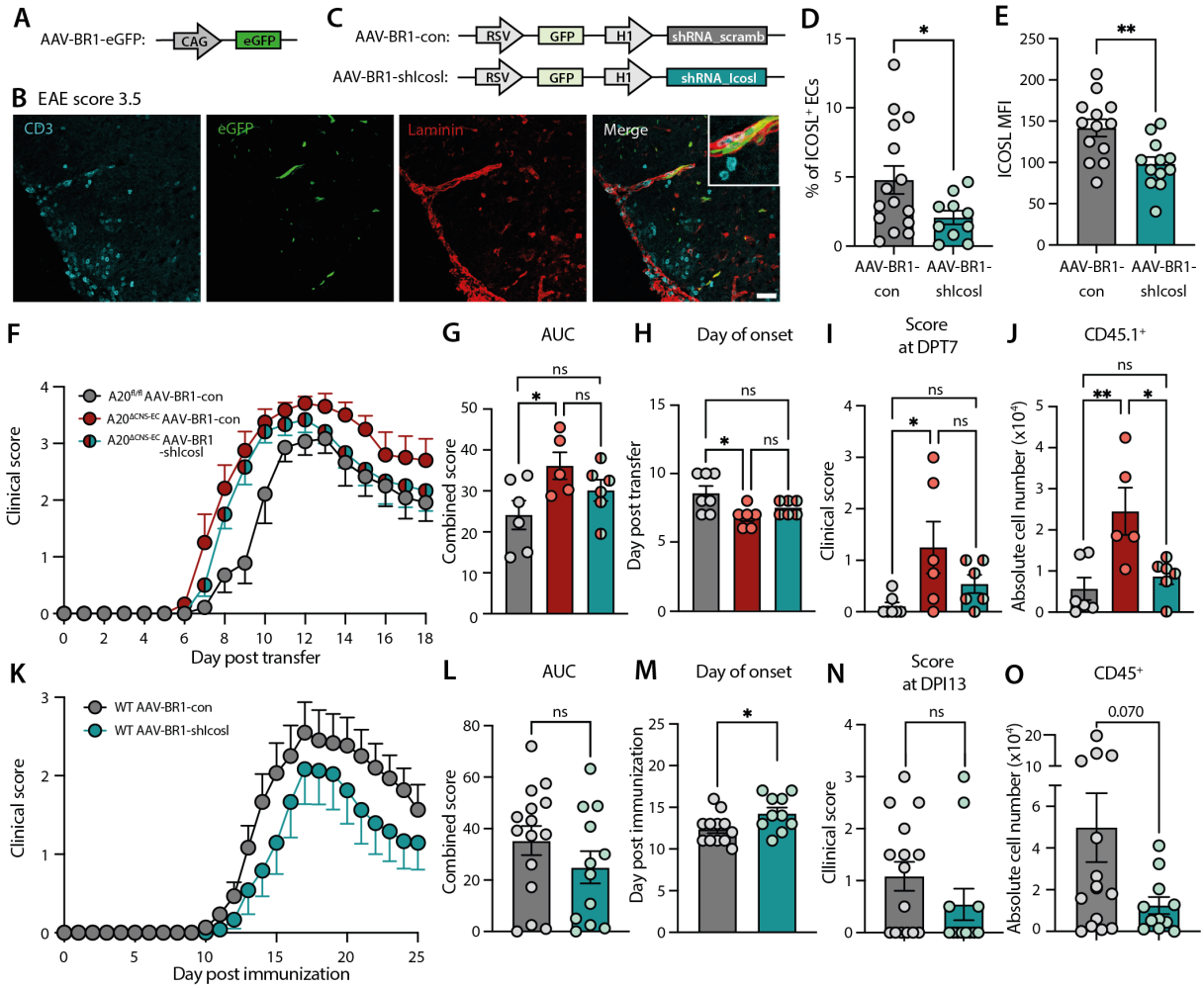

Figure 6: Knockdown of ICOSL on CNS microvascular ECs mildly ameliorates EAE severity
(A) Schematic representation of AAV-BR1-eGFP construct. (B) Representative immunofluorescence of SC tissue from mice treated with AAV-BR1-eGFP. Tissue was harvested at peak of EAE disease and stained for CD3 (cyan) and laminin (red). Endogenous eGFP is shown in green. Scale bar = 40 µm. (C) Schematic representation of AAV-BR1 constructs. (D) Percentage of ICOSL$^+$ ECs and (E) MFI (geometric mean) of ICOSL on brain ECs in wildtype mice treated with AAV-BR1 constructs and two weeks later immunized with MOG/CFA. Analysis was performed at DPI10. Data is pooled from 2 individual experiments with n = 10-15 mice per group. (F-J) A20$^{\Delta CNS\text{-}EC}$ or A20$^{fl/fl}$ controls were treated with AAV-BR1-shIcosl or AAV-BR1-con as indicated. One week later, mice were treated with TAM and AT-EAE was induced four weeks later (n = 5-7 mice per group). (F) Clinical signs were monitored daily and are shown as mean clinical scores +/- SEM. (G) AUC, (H) day of onset and (I) score at DPT7 analyses from data shown in (F). (J) Flow cytometric analysis of CD4$^+$ CD45.1$^+$ transferred T cells in the SC at DPT18. (K-O) Wildtype mice were injected with AAV-BR1 constructs. Two weeks later, mice were immunized with MOG/CFA. (K) Clinical signs were monitored daily and are shown as mean clinical scores +/- SEM. Data is pooled from 2 independent experiments with n=12-15 mice per group. (L) AUC and (M) day of onset and (N) score at day post immunization (DPI) 13 analyses of clinical course shown in (K). (O) Flow cytometric analysis of CD45$^+$ in the SC at DPI30. Statistical significance was determined by two-tailed unpaired Student's t-test (L-O) or ordinary one-way ANOVA with Tukey's multiple comparisons test (G-J). ns = not significant, * p<0.05, ** p<0.01.

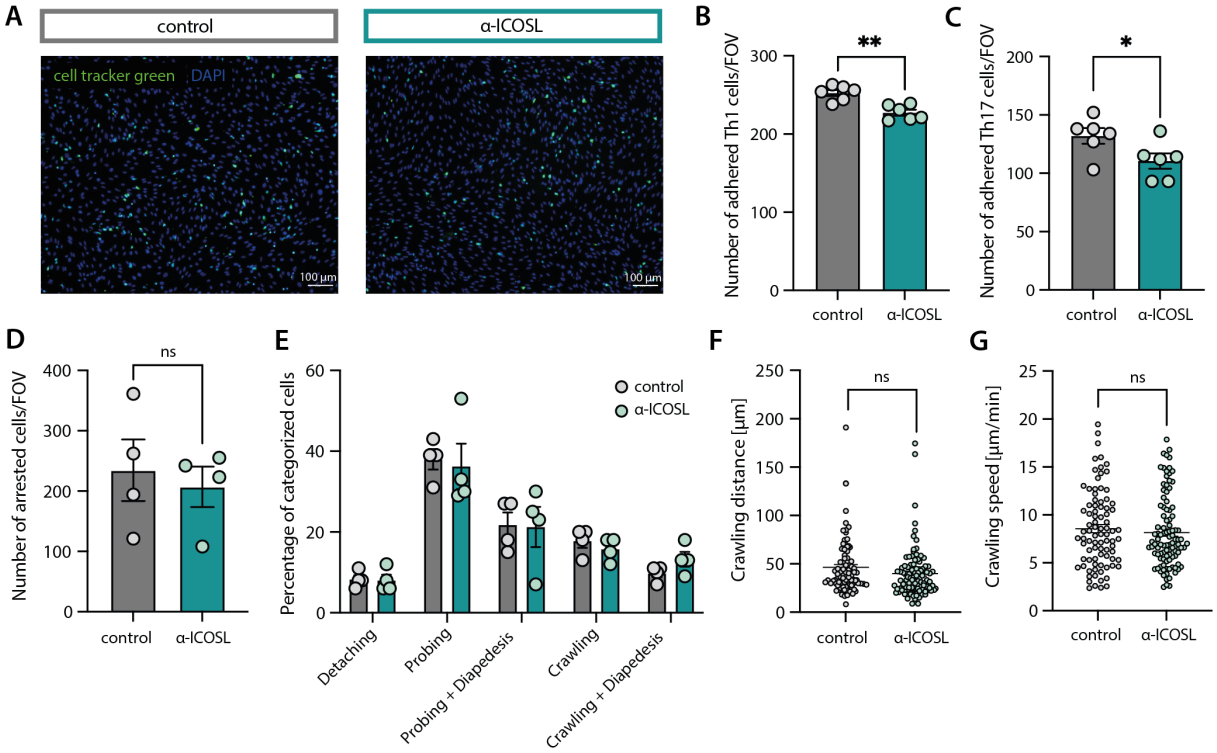

Figure 7: ICOSL regulates T cell adhesion to pMBMECs

(A-C) Static adhesion assay of T cells on pMBMECs. pMBMECs were stimulated with IL-1β for 72 h and incubated for 30 min with α-ICOSL or control antibody. T cells were labelled with CellTracker™ Green CMFDA dye and added for 30 min to the pMBMECs on a shaking platform. After washing, images were taken and adhering cells were counted. Data is representative for 2 individual experiments with n = 6 per group. (A) Representative microscopic images of 2D2 Th1 cells (green) adhering to the pMBMEC monolayer (nuclear stain blue, DAPI). (B) Quantification of number of adhered 2D2 Th1 cells per field of view (FOV). (C) Quantification of number of adhered 2D2 Th17 cells per FOV. (D-G) Analysis of T cell post-arrest behavior on pMBMECs. Data is pooled from 4 individual experiments. pMBMECs were stimulated with IL-1β for 72 h and incubated for 30 min with α-ICOSL or control antibody. 2D2 Th1 T cell post-arrest behavior was assessed by live cell imaging under physiological flow. (D) Number of arrested Th1 cells per FOV. (E) Quantification of T cell post-arrest behavior. Each category is shown as fraction of the sum of the categorized cells. (F) Crawling distance of T cells that successfully completed diapedesis on IL-1β-stimulated isotype or α-ICOSL treated pMBMECs under flow conditions during 20 min observation time shown in µm. (G) Crawling speed of T cells that successfully completed diapedesis on IL-1β-stimulated isotype or α-ICOSL treated pMBMECs under flow conditions shown in µm/min. Data in (F) and (G) is pooled from 4 individual experiments with n = 86-102 tracks analyzed. Data was analyzed using two-tailed unpaired Student's t-test (B-D, F, G) or two-way ANOVA with Šidák's multiple comparison test (E). ns = not significant, * $p<0.05$, ** $p<0.01$.